The Thesis committee for Xinyue Tong

Certifies that this is the approved version of the following thesis:

SINGLE-CRYSTAL ELASTICITY OF THE LOWER-MANTLE FERROPERICLASE ($Mg_{0.92}Fe_{0.08}$)O

APPROVED BY

SUPERVISING COMMITTEE

Supervisor: _____
Jung-Fu Lin

_____
Luc L Lavier

_____
Stephen P Grand

SINGLE-CRYSTAL ELASTICITY OF THE LOWER-MANTLE FERROPERICLASE ($Mg_{0.92}Fe_{0.08}$)O

by

Xinyue Tong, B.A.

Thesis

Presented to the Faculty of the Graduate School of

The University of Texas at Austin

in Partial Fulfillment

of the Requirements

for the Degree of

Master of Science in Geological Sciences

The University of Texas at Austin

May 2014

Acknowledgements

At this moment, I would like to give my deep appreciation to my supervisor Professor Jung-Fu Lin, for his guide and support, and also for his valuable advice both on my study and my future plan. Secondly, I would like to give equal appreciation to my co-worker Jing Yang. She prepared all of cells that we need and did many analyses on the data. She did a great job on her part of this project. Without her selfless helps, I could not finish my project this smooth and quick.

Moreover, I would like to give thanks to my officemate Jin Liu and his wife Hailing Gu, and my previous roommate Chang Lu, for treating me like a family and making my life in Austin colorful.

Last but not least, I would like to give thanks to my family. Thanks to my beloved wife Qiaoyun Ma, for her love, understand and support. I would not reach my goal without her. And thanks to my parents for their encouragements and led me my way to Science.

Abstract

SINGLE-CRYSTAL ELASTICITY OF THE LOWER-MANTLE FERROPERICLASE ($Mg_{0.92}Fe_{0.08}$)O

Xinyue Tong, M.S. Geo. Sci.

The University of Texas at Austin, 2014

Supervisor: Jung-Fu Lin

This study focuses on investigating the effect of the electronic spin transition of iron on the elasticity of the candidate lower mantle ferropericlase (Mg,Fe)O. This may be relevant to our understanding of the seismic velocity structures of the Earth's lower mantle. The elastic constants of ($Mg_{0.92}Fe_{0.08}$)O at high-spin (HS) state, low-spin (LS) state, and through the pressure-induced HS-to-LS transition was measured using both Brillouin Light Scattering (BLS) and Impulsive Stimulated Scattering (ISS). There was a large pressure range in which c_{11} and c_{12} exhibited a softening, while c_{44} did not register such an anomaly. Compared with previously published data of ferropericlase with similar compositions [Crowhurst et al., 2008; Marquardt et al., 2009b], this study provides more reliable elastic constants measurements by taking advantage of simultaneous measurements on Vp and Vs using both BLS and ISS. Our results show that bulk sound velocities of ferropericlase have a large but smooth softening in the spin transition pressure region. The elastic constants of ferropericlase at the spin transition region and

the LS state were well studied in this thesis, and a relaxation behavior was also been observed in this study. Those subjects are not well documented in the current literature. The temperature effect of the spin state transition and its consequential effect on the elastic properties of ferropericlase were not studied in this project. Further research on this subject will follow. However, even in the room temperature, our results did not show sudden changes in seismic velocities. Moreover, current theoretical and experimental studies [Sturhahn et al., 2005, Tsuchiya et al., 2006, Lin et al., 2007] indicate that the spin transition takes place over an extended range of depth along an expected lower-mantle geotherm, where sudden changes in compressional and bulk sound velocity are not expected.

Contents

CHAPTER 1 INTRODUCTION

The earth's lower mantle is the largest layer of the Earth's interior in terms of volume. Based on pyrolite mode, it mainly contains ~20% ferropericlase (Mg,Fe)O, ~75% aluminous silicate perovskite Al-(Mg,Fe)(Si,Fe)O_3, and ~5% calcium silicate perovskite $CaSiO_3$ [Ringwood, 1982; Irifune 1994; Irifune and Isshiki, 1998; Irifune et al., 2010]. Silicate post-perovskite (Mg,Fe)(Si,Fe)O_3, which transitions from silicate perovskite at the lowermost mantle P-T condition, is thought to be stable only in the D" region just above the core-mantle boundary (CBM) [Murakami et al., 2004; Oganov and Ono, 2004; Hirose, 2006] (Figure 1.1). Under the pressure and temperature conditions of the Earth's lower mantle, the electronic configuration of iron can be changed dramatically, inducing an electronic spin-pairing transition. This transition affects the physical and chemical properties of the iron-bearing mantle materials. To date, the interpretation of seismic observations gives us the clearest picture of the structure and dynamic of the Earth's lower mantle. However, detailed knowledge of the candidate lower mantle minerals' physical properties under relevant P-T condition is needed for seismic wave velocity interpretations. Ferropericlase is the second most abundant mineral in the lower mantle. Thus, understanding its elastic properties in high-spin state, low-spin state, and spin crossover is essential.

The first report on how spin transition affects sound velocities of (Mg,Fe)O was studied by Lin et al. (2006) using Nuclear Resonant Inelastic X-Ray Scattering (NRIXS) in a Diamond Anvil Cell (DAC). Across the spin transition, the derived Vp and Vs show

significant changes; however, the value of those velocities are lower than other studies with different experimental methods.

Crowhurst et al. (2008) reported the first direct acoustic compressional wave velocity measurement of single-crystal ferropericlase ($Mg_{0.94}$,$Fe_{0.06}$)O over the electron spin-pairing transition in iron using the Impulsive Stimulated Light Scattering (ISS). Their results (Figure 1.2) show a large velocity reduction on compressional waves but only a small decrease on interfacial wave over the spin transition region. This technique does not have sensitivity to shear wave measurement; shear wave was derived from interfacial wave velocity with many assumptions including the elastic properties of the pressure medium. The elastic constants, c_{ij}, derived from this study were not very reliable, especially for c_{44} which is directly related to the shear wave velocity propagate along [100] on the (100) plan.

Recently, the Brillouin Light Scattering technique (BLS) has been used to measure the elasticity of ($Mg_{0.9}$,$Fe_{0.1}$)O single crystal [Marquardt et al., 2009a], which indicates no marked decrease in shear velocity (Figure 1.3) over the spin transition region. Compressional wave velocities cannot be measured at higher pressure using the technique (starts at 32 GPa), as it is embedded into the diamond's shear wave peak on the Brillouin spectrum. Marquardt et al. (2009a) used shear constant $(c_{11} - c_{12})/2$ and adiabatic bulk modulus (calculated from X-ray diffraction data) to determine the c_{11} and c_{12} above 32GPa. The uncertainties for those indirectly measured elastic constants are relatively large. Thus far, the elasticity of ferropericlase in the low-spin state and the spin transition region remains largely unresolved.

The study reported in this thesis is the first attempt to measure compressional and shear wave velocities of ferropericlase, simultaneously, up to the Earth's lower mantle conditions. I present the experimental studies of single-crystal ferropericlase containing 8at.% Fe, $(Mg_{0.92}Fe_{0.08})O$, using both Impulsive Stimulated Light Scattering (sensitive to compressional wave) and Brillouin Light Scattering (shear wave can be directly measured). Therefore, this study overcomes the limitation of each individual technique. All elastic constants, c_{11}, c_{12}, and c_{44} are determined from direct measurements. Reliable acoustic wave velocities are measured up to 89 GPa. In Sec. 1.1, I give a brief description of the general features of the spin transition in ferropericlase. A brief overview of this thesis is in Sec. 1.2.

1.1 General Features of the Spin Transition in Ferropericlase

Iron is the most abundant transition metal on Earth. Its 3d electronic shells are partially filled. Ferrous iron (Fe^{2+}, the major iron cation in ferropericlase) has 6 electrons in the 3d shells. Those electrons occupy the relative high-energy doublet e_g orbitals and relative low-energy triplet t_{2g} orbitals differently in the octahedral site of ferropericlase. Factors such as pressure can alter the occupation of those electrons in the 3d shells of iron (Figure 1.4). For the octahedral site of ferropericlase, under ambient conditions, the 3d electrons are more likely to occupy different orbitals with the same electronic spin in which four of them are unpaired electrons and two are paired electrons; this is the high-spin state. In this case, the crystal-field splitting energy which separates the e_g and t_{2g} orbitals is lower than the electronic spin-pairing energy. Under high pressure, the crystal-field splitting energy overruns the spin-pairing energy, and this causes the pairing of the

3d electrons of the opposite spin in which all six paired electrons are occupied the t_{2g} orbitals, this is called the low-spin state [Lin et al., 2013].

The pressure induced spin transition of Fe^{2+} in ferropericlase has been reported to occur over a narrow pressure range of 40-60 GPa at room temperature from various experimental studies and theoretical calculations. However, at relevant pressure-temperature conditions of the Earth's lower mantle, the effects of the spin crossover of iron are expected to occur over a broader pressure range than those at ambient temperature condition [Badro et al., 2004; Lin et al., 2005; Lin and Tsuchiya, 2008; Lin et al., 2013].

1.2 Overview of the Thesis

In this thesis, I describe one of the applications of Impulsive Stimulated Light Scatting (ISS) technique in the research of the elastic behaviors of ferropericlase at Earth's lower mantle conditions. I first present the ISS technique. Following that, I present the application of the ISS technique on single crystal $(Mg_{0.92}Fe_{0.08})O$ acoustic wave velocity measurements and discuss the geophysical implications of the electron spin-pair transition of iron in ferropericlase under the Earth's lower mantle condition based on the analyses of experimental data (combined with Brillouin Light Scattering measurements) and literature reports.

Chapter 2 contains a description of the implementation of the ISS technique, the excitation mechanisms, probing techniques, and the system calibrations.

In Chapter 3, I describe the sample synthesis process and experimental details of unit cell volume and compressional and shear wave velocity measurements up to 89GPa at room temperature.

Chapter 4 contains the results and analysis of the experimental data, including the spin state, bulk modules, bulk sound velocity, density, and elastic constants.

In Chapter 5, I discuss the geophysical implication from our findings and draw conclusions from results that I present in this thesis.

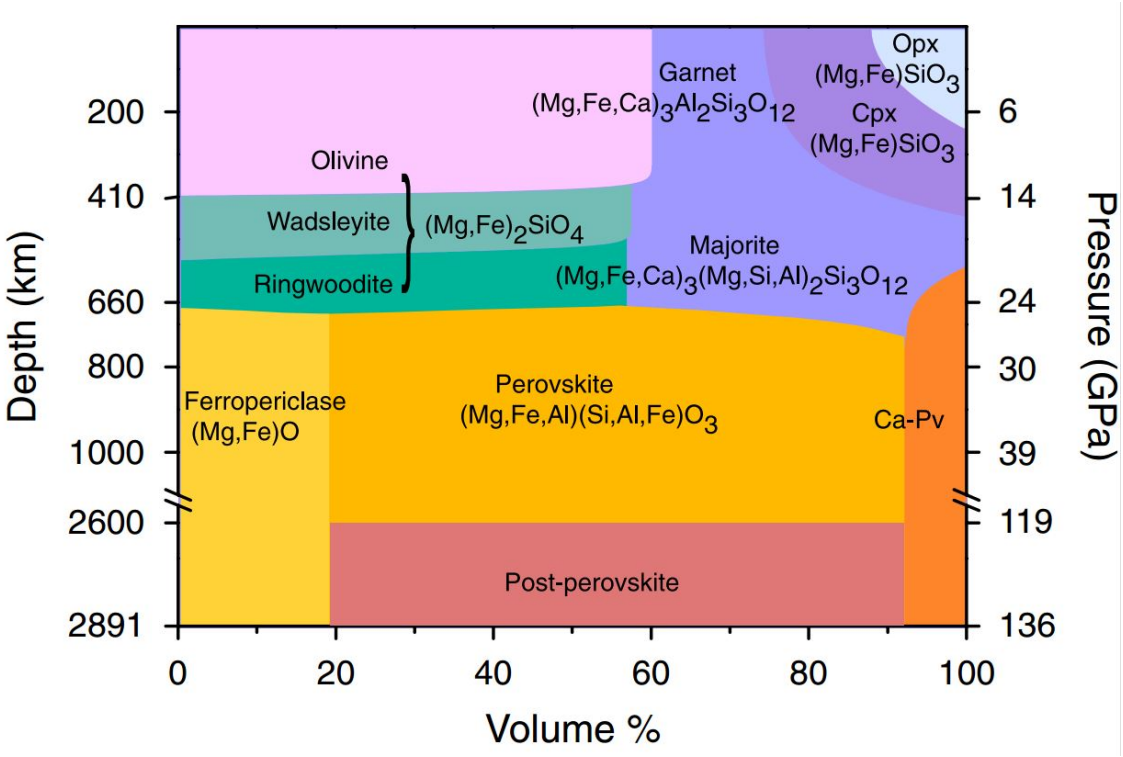

Figure 1.1 Mineralogical model of the Earth's interior as a function of depth (pressure) [Lin et al., 2013]. Mineral abbreviation: Opx and cpx, orthopyroxene and clinopyroxene, respectively; CaPv, calcium silicate perovskite.

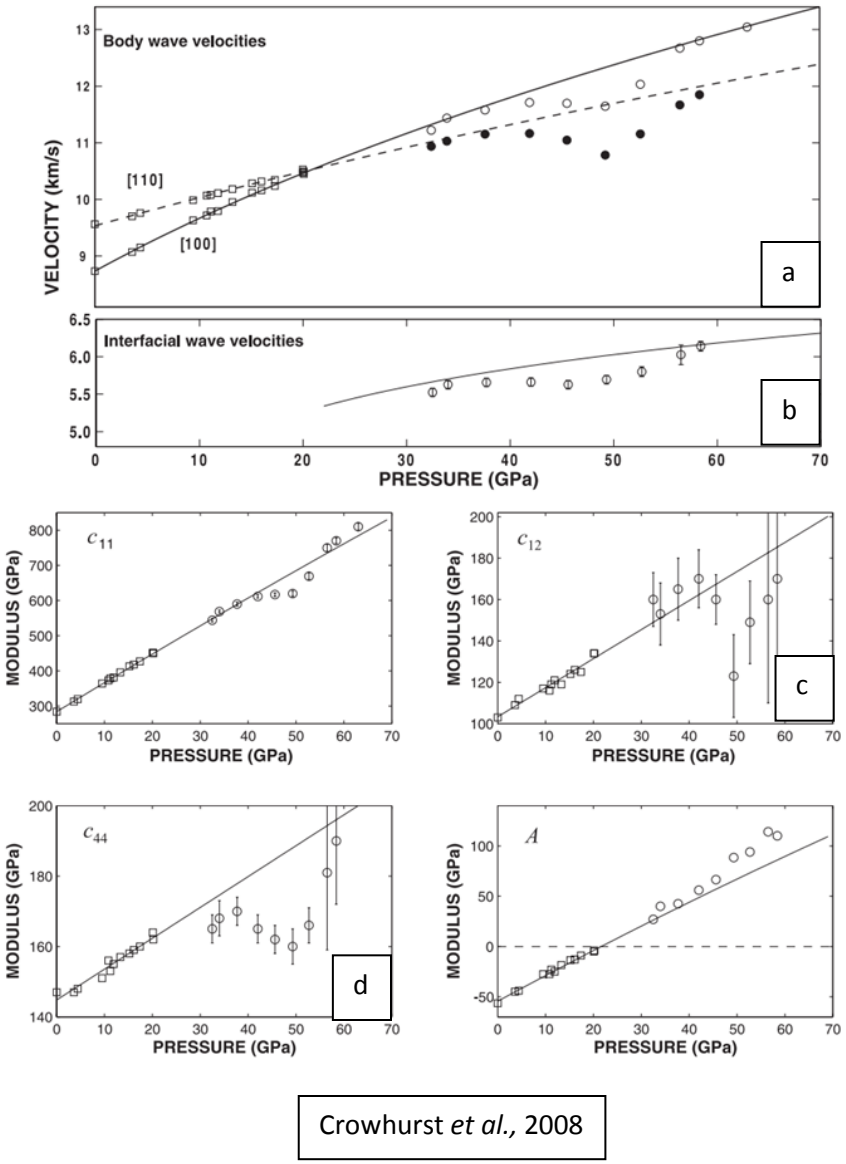

Crowhurst *et al.,* 2008

Figure 1.2 Impulsive Stimulated Light Scattering (ISS) study of single crystal ferropericlase $(Mg_{0.94},Fe_{0.06})O$ by Crowhurst et al. (2008) . Their results show a large velocity reduction on compressional wave (a) but only a small decrease on interfacial wave (b) over the spin transition region. The shear wave velocities couldn't be measured directly by this technique but were rather calculated from interfacial wave velocity with many assumptions, like pressure medium elastic properties. The elastic constants, c_{ij}, derived from this study were not very reliable. Especially c_{12} (c) and c_{44} (d) which directly relate to the shear wave velocity propagate along [110] and [100] on the (100) plan.

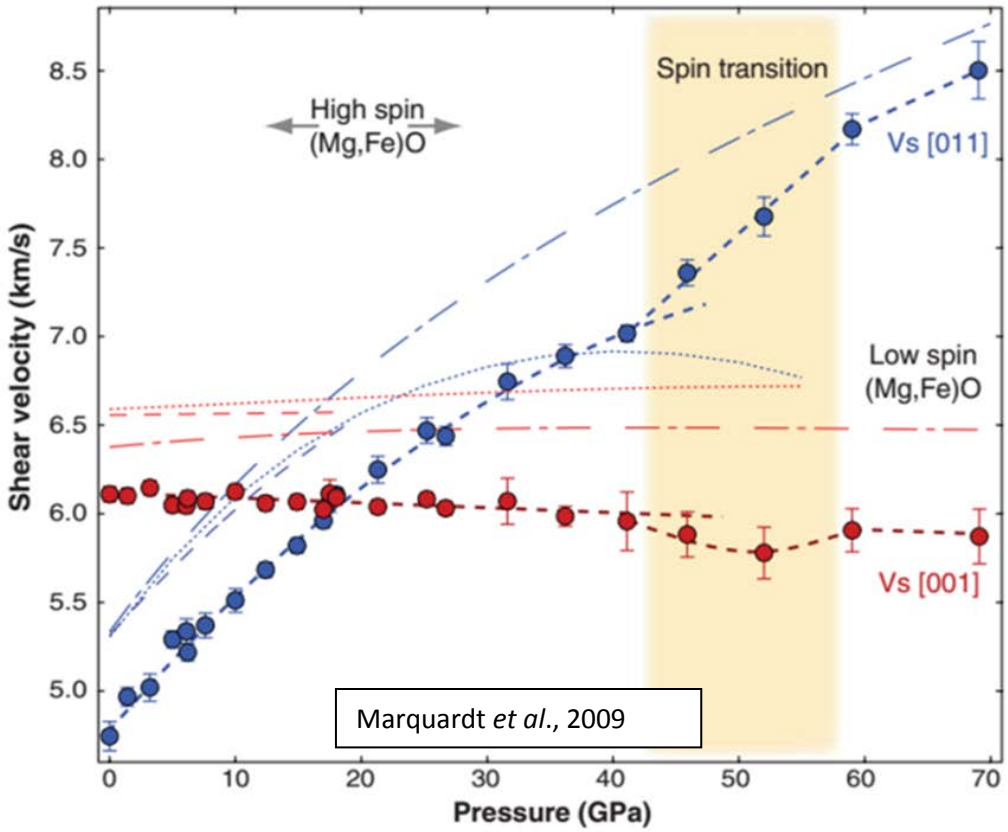

Figure 1.3 Brillouin Light Scattering technique has been used to measure the acoustic velocity of $(Mg_{0.9},Fe_{0.1})O$ single crystal [Marquardt et al., 2009a], which indicates no marked decrease in shear velocity over the spin transition region. Compressional wave velocities cannot be measured at a higher pressure (start at 32 GPa), as it is embedded into diamond's shear wave peak on Brillouin spectrum.

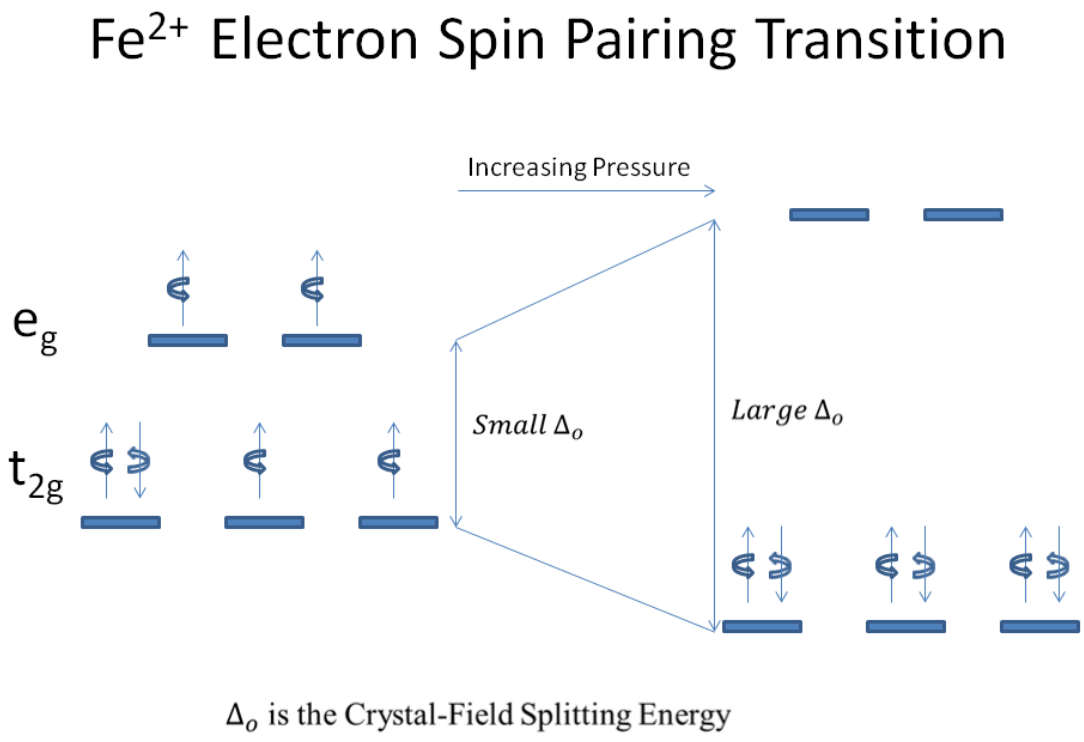

Figure 1.4 Under ambient conditions, the Fe^{2+} 3d electrons in ferropericlase are more favorable to occupy different orbitals with the same electronic spin in which four of them are unpaired electrons and two are paired electrons; this is the high-spin state. In this case, the crystal-field splitting energy which separates the e_g and t_{2g} orbitals is lower than the electronic spin-pairing energy. With increasing pressure, the crystal-field splitting energy increases with the spin-pairing energy, and this causes the pairing of the 3d electrons of the opposite spin in which all six electrons are paired, this is called the low-spin state.

CHAPTER 2 IMPULSIVE STIMULATED LIGHT SCATTERING TECHNIQUE

2.1 Introduction

An impulsive stimulated light scattering is a time-resolved optical spectroscopy method. It has a long working history in physics, chemistry, material science, and mechanical engineering researches. Recently, it shows powerful capabilities in Earth and Planetary Science researches. It can be used to study the elastic, thermodynamic, and transport properties of crystals and fluids at high temperature and pressure conditions [Abramson et al., 1999]. In this Chapter, I describe details of the experimental implementation of the ISS technique at UT Austin Mineral Physics Lab.

2.2 The Technique

Impulsive stimulated light scattering is a time delay "transient grating" process. It has been explained in details by Yan et al. (1987). I will briefly describe the technique base on our current experimental interests in the mineral physics lab at The University of Texas At Austin (see Appendix I for brief discussion of thermal diffusivity and surface wave measurements as well as heterodyning detection technique). Fig. 2.1 shows a schematic illustration of ISS experiment as conducted this thesis. Two parallel-polarized, picosecond excitation pulses of wavelength λ_E are crossed at an angle of intersection $\theta_C = 2\theta$ and overlapped spatially and temporally inside the sample. The optical interference of these two pulses creates an intensity grating pattern with wavevector magnitude $q = \frac{4\pi\sin(\theta)}{\lambda_E} = \frac{2\pi}{d}, d = \frac{\lambda_E}{2\sin(\theta)}$, where d is the interference fringe spacing. It is also the wavelength of the acoustic wave that was generated in the sample. When a third

probe beam is incident at the phase-matching (Bragg) angle ($\theta/2$) for the grating, part of the probe light will be diffracted in a direction with the mirror symmetry of the transmitted probe light (Figure 2.2). The time dependence of the material excitations is obtained by recording the diffraction efficiency as a function of the time delay between excitation and probe pulse beams.

Excitation pulses can interact with the sample in two ways. First, acoustic modes can de excited through an impulsive stimulated Brillouin scattering (ISBS). In this mechanism, the electric field exerts a sudden ("impulsive") electrostrictive stress with wavevector $\pm q$. Second, absorption of the excitation light by the sample can occur. For absorbing materials, optical absorption at the intensity peaks and subsequent rapid thermalization leads to the sudden formation of a temperature grating with wavevector q. Thermal expansion due to this impulsive, spatially periodic heating then results in a time-dependent density response at this wavevector. This process is referred to as an impulsive stimulated Thermal scattering (ISTS). In this case, not only the acoustic mode but also the thermal diffusion mode can be excited [Nelson and Fayer, 1980; Nelson et al., 1981; Yan et al., 1987]. However, the thermal decay (in Milliseconds) is much longer than acoustic decay (in Nanoseconds) in time scale [Abramson et al., 1999].

As far as the excitation of acoustic dynamics is concerned, there is no difference between the ISBS and ISTS mechanisms, as both of them give the same acoustic frequency. The acoustic mode can always be excited through an ISBS for absorbing or non-absorbing materials, while only absorbing materials gives an ISTS signal. However, an ISTS signal is much stronger than an ISBS signal with the same excitation Laser

intensity [Nelson and Fayer, 1980; Nelson et al., 1981; Yan et al., 1987]. An ISBS contribution is negligible in our experiment setup.

2.3 The System Setup

Fig. 2.3 schematically shows the experimental implementation of the ISS system in the Mineral Physics lab at the University of Texas at Austin. Both excitation and probe pulses have the 15ps pulse width with up to a 200,000 Hz repetition rate. The 1064nm wavelength Inferred Laser severs as the excitation beam. It has been polarized and split with a 50/50 beam-splitter into two excitation pulses that are focused and crossed at an excitation angle 2θ. These two pulses are temporally and spatially overlapped inside the sample by adjusting the relative path length and mirror position. The 532nm wavelength green Laser severs as the probe beam. This probe pulse is incident upon the center of the grating at a Bragg angle. The time delay between the excitation and the probe pulses is controlled mechanically by moving the retroreflector on the translation stage. The 5 feet long translation stage and the 4 rebound paths can provide a total time delay up to 20ns.

The signal beam is directed into a photodetector with a short raise time of approximately 14ns. The output of the photodeector is sent to a lock-in amplifier whose reference frequency is synchronized with an optical chopper running at a frequency less than the repetition rate of the excitation and the probe beams. The chopper is placed in the path of one of the excitation pulses to reduce the scattered light from the probe beam. A 532nm centered bandpass glass filter places in front of the detector to minimize the noise from excitation beams. The lock-in amplifier is connected through a general

purpose interface bus (GPIB) interface to a computer interface, which also controls the time delay of the probe pulse via the moving of the translation stage (See Appendix II for details on instrumentation of the ISS). For each given delay time between the excitation and probe pulses, the computer records the diffracted signal intensity from the lock-in amplifier. All instrumental controlling and signal recording are programmed integrally on the platform called LabView (Fig. 2.4).

As an ISS signal level is proportional to the peak power in a probe beam; compare to other continuous laser probing techniques, this pulse laser detection technique has very high signal intensity. However, the data collection time is longer as each laser shot only yields just a point on the time axis rather than the entire temporal response.

2.4 The System Calibration

The crossing angle of two excitation pulses is calibrated by using the standard sample of HOYA HA-50 heat absorbing glass (see Appendix III for the glass information provided by the manufactory) and distilled water. Compression wave velocities of glass and water are measured by Brillouin light scattering system. In an ISS, the frequency of the compression wave can be obtained after transform the recorded measurements from time domain to frequency domain.

$d = \lambda_A = \frac{\lambda_E}{2\sin(\theta)}$, and $v = f\lambda$, where d is the space between interference and the acoustic wavelength λ_A is defined by d. The wavelength of excitation beams, λ_E, is 1064nm and θ is the half of the excitation beams crossing angle. f is the frequency of compression waves, and v is the compression wave velocity. Therefore, the angle

between two excitation beams, θ_C, is $\theta_C = 2\theta = 2\sin^{-1}(\frac{f}{v}\frac{\lambda_E}{2})$, which again, f and v are measured from ISS and BLS, and λ_E is 1064nm. The current crossing angle is 20.3 ± 0.6.

Figure 2.5 shows the representative glass and water ISS measurements in time domain and their power spectrums in frequency domain.

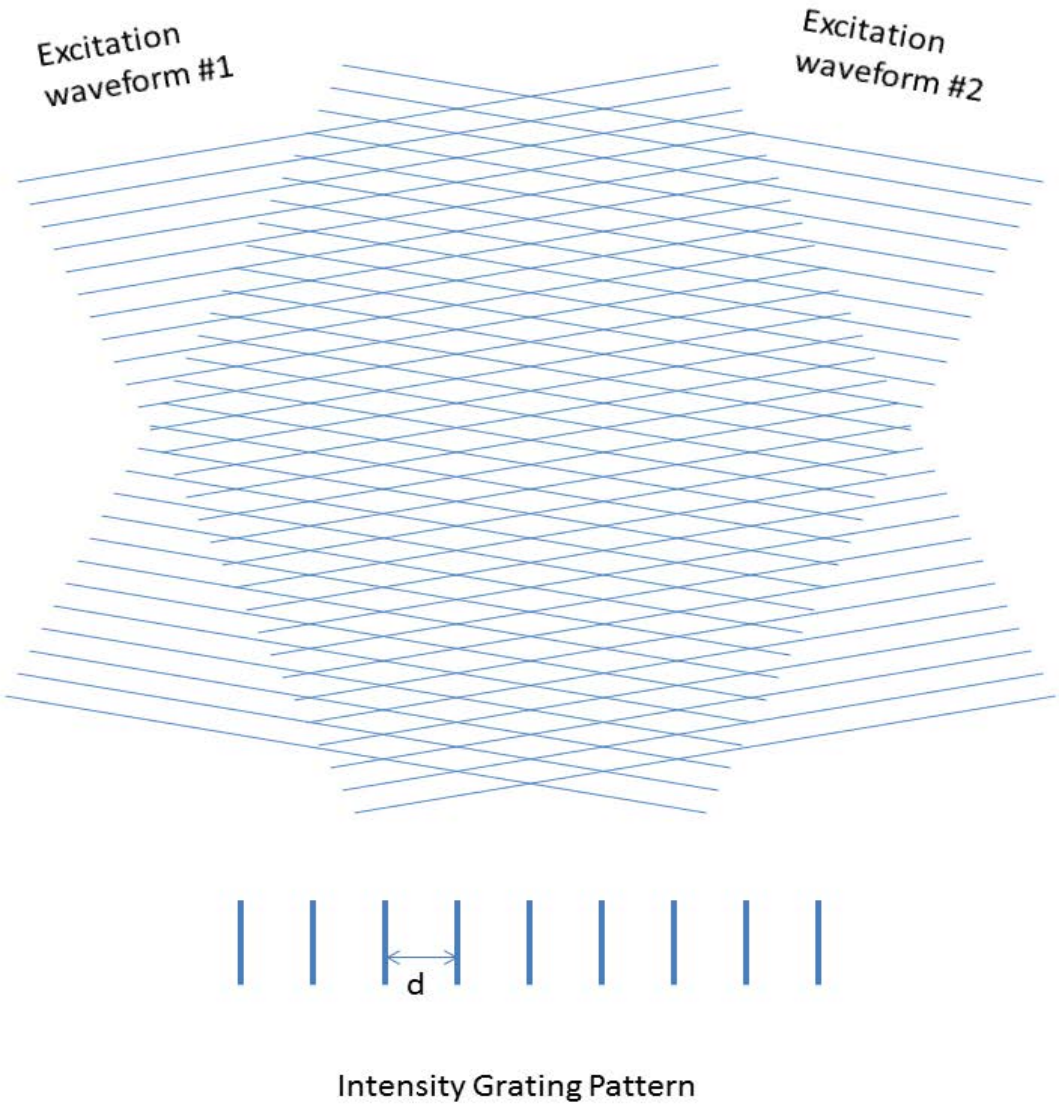

Figure 2.1 Formation of the interference grating pattern by crossing two excitation pulses. The spacing, $d = \frac{\lambda_E}{2\sin(\theta)}$, between each fringe defined the wavelength of acoustic wave that are propagating across the sample. λ_E is the wavelength of excitation beam, and θ is the half of the angle between two excitation beams [Nelson and Fayer, 1980; Nelson et al., 1981; Yan et al., 1987; Abramson et al., 1999].

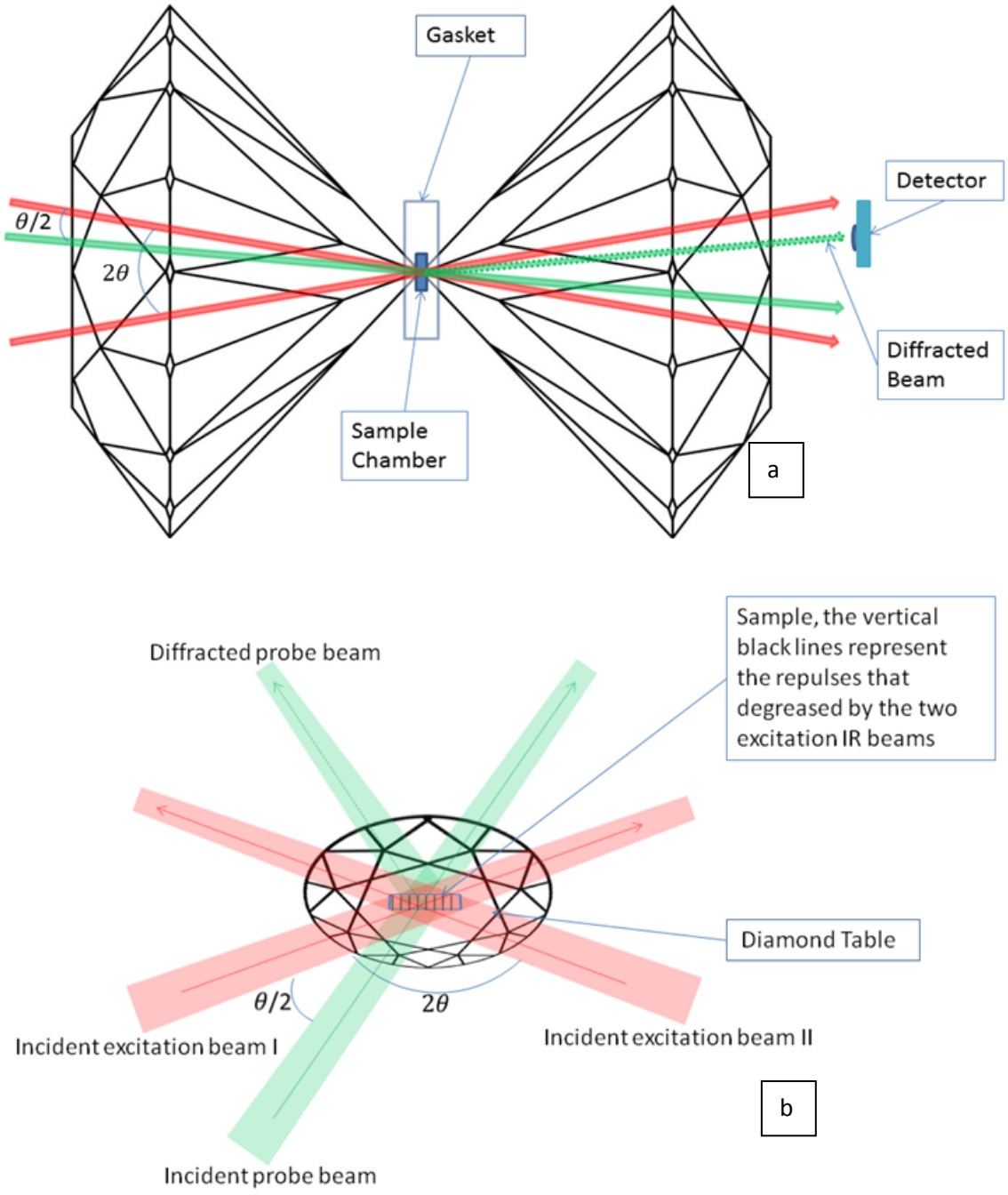

Figure 2.2 Diamond Anvil Cell, pump (Red) and probe (Green) beams geometry. (a) side view. (b) view from diamond table.

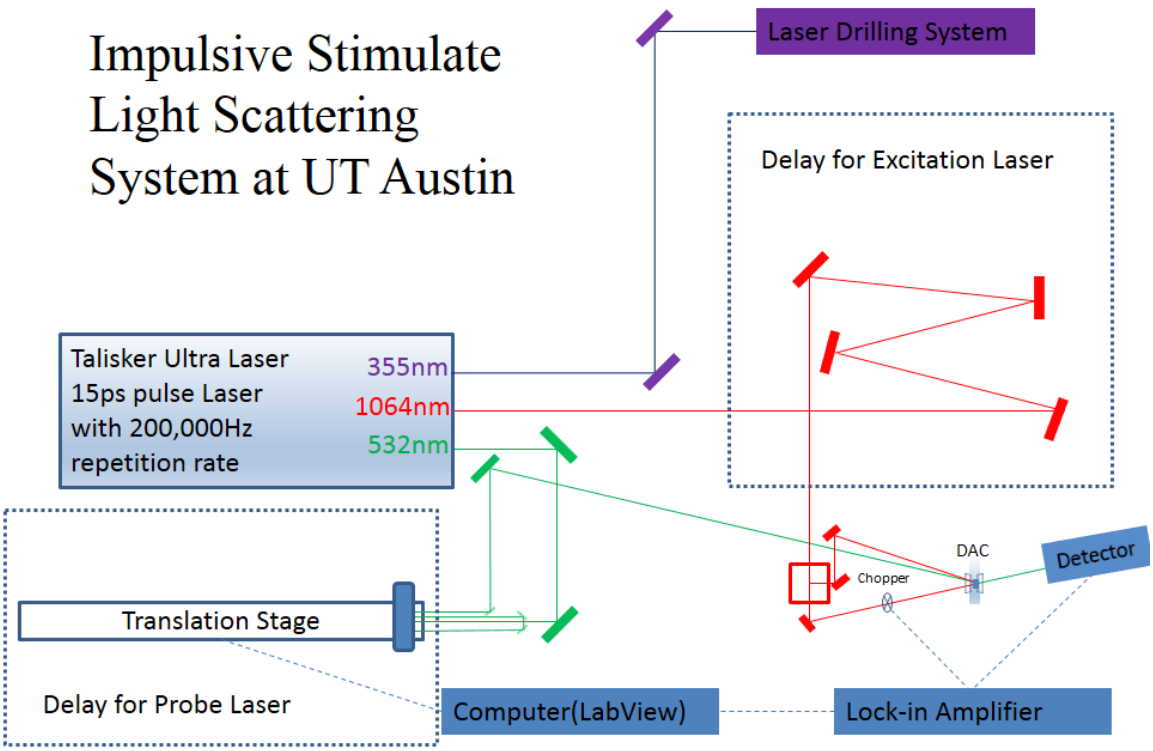

Figure 2.3 Schematic of the Impulsive Stimulated Light Scattering setup in the Mineral Physics Lab at The University of Texas at Austin. It is equipped with a Coherent Talisker Ultra Laser system, a PD Detector, a Lock-in Amplifier, a Translational Stage for elasticity measurements, and a computer to control the whole system through LabView (See Appendix I for details on instrumentation of the ISS).

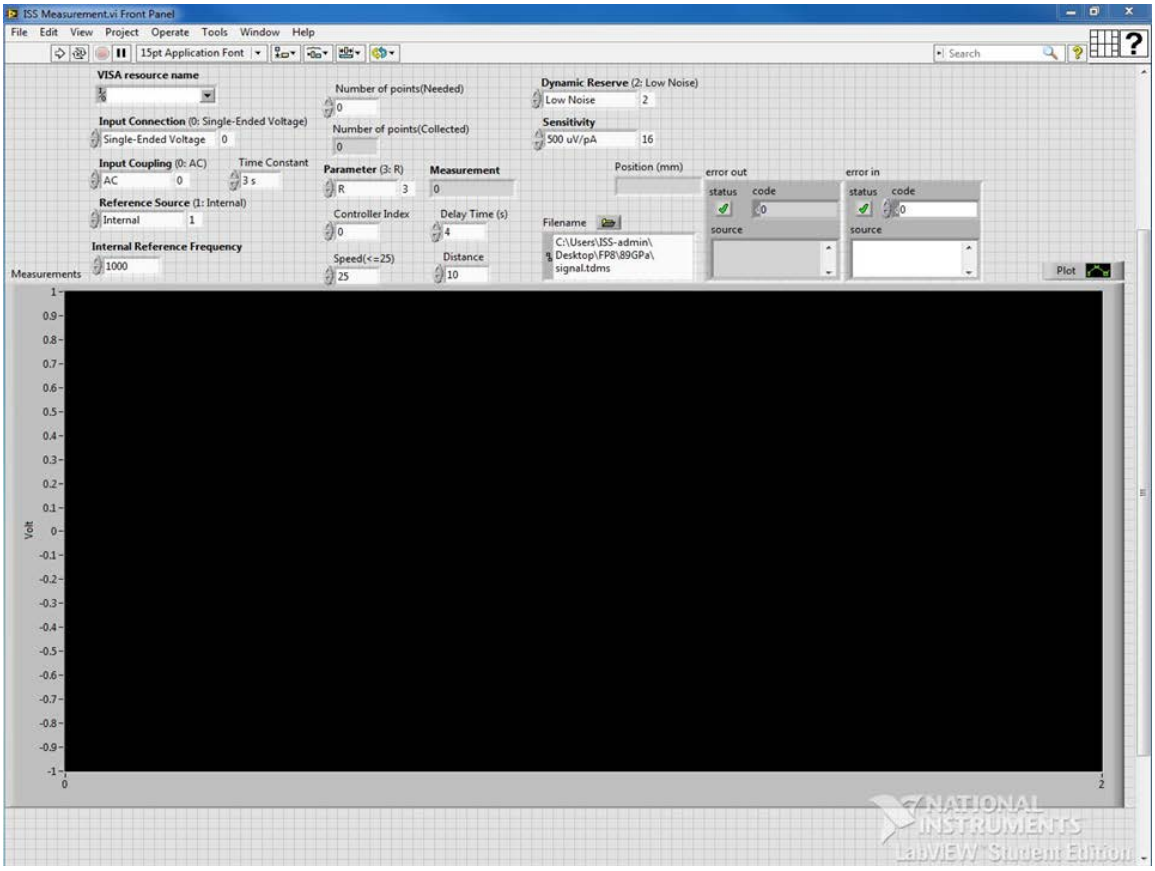

Fig. 2.4 The control interface build on LabView, all instrument controlling and signal recording are programmed integrally on this platform.

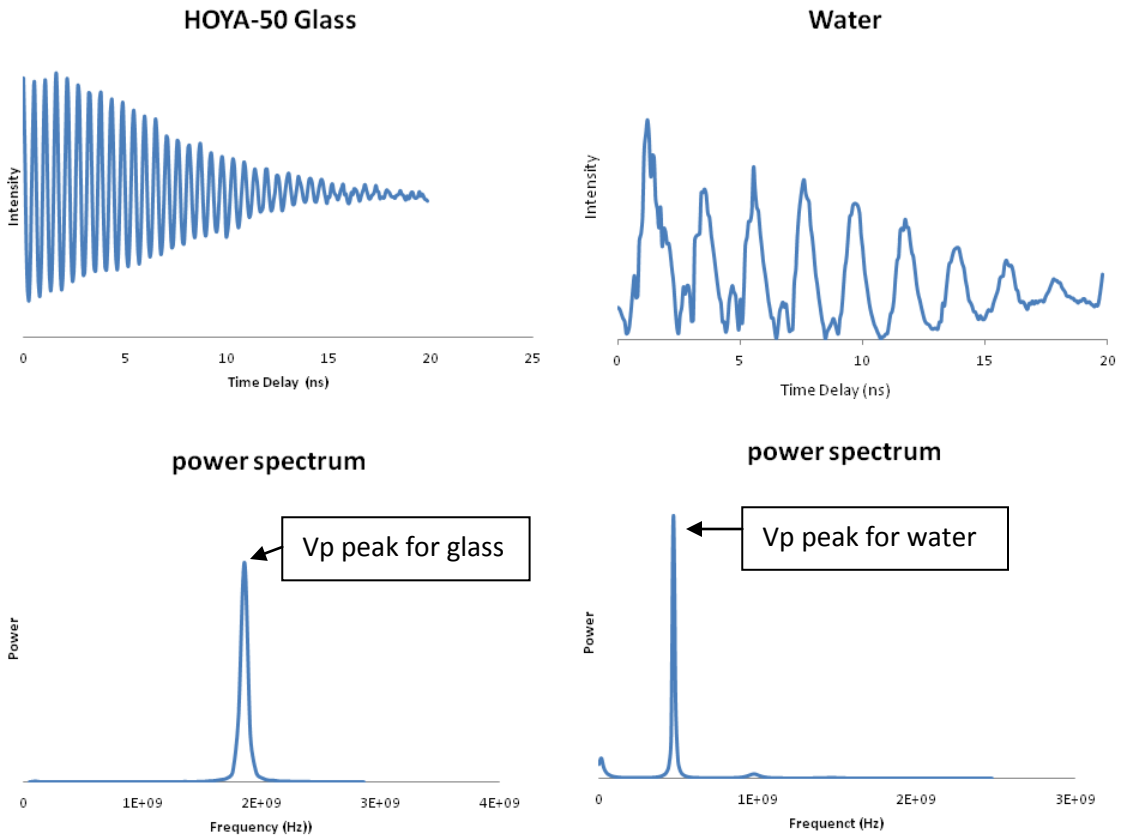

Figure 2.5 Calibration of the ISS system using glass and water standards. **Left**, Glass ISS measurement in time domain and its power spectrum in frequency domain; **Right**, Water ISS measurement in time domain and their power spectrum in frequency domain. Those are used for ISS system calibration purpose. Glass and water Vp were calibrated with BLS measurements. The BLS system was calibrated using the elastic constants of standard silicate glass, distilled water, and single-crystal MgO [Ostwald et al., 1977; Sinogeikin and Bass, 2000; Polian et al., 2002]

CHAPTER 3 MATERIALS AND METHODS

3.1 Sample Material

The ferropericlase sample was synthesized by Prof. Jung-Fu Lin in collaboration with Dr. Okuchi and Dr. Tomioka at the Institute for Study of The Earth's Interior (ISEI) Okayama University in Misasa. Briefly, the ferropericlase sample was synthesized by inter-diffusion of Fe and Mg between single crystal periclase (pre-aligned to (100) crystallographic plane) and prereacted (Mg, Fe)O powder in a gas furnace operating at 1450 °C and 10^{-2} Pa oxygen fugacity for 10 days. The chemical formula for this sample was analyzed by Electrical Microprobe in the E-Beam Lab at the Jackson School of Geosciences to be $(Mg_{0.92}Fe_{0.08})O$ (Fp8). Hereafter we will refer to this sample as Fp8. Sample platelets were double polished down to approximately 15μm thick in (100) platelets.

3.2 X-ray Diffraction

The single crystal X-ray diffraction experiment was performed by Jing Yang at the Sector 13BMD, GSECARS sector of the Advanced Photon Source (APS), Argonne National Lab (ANL). The experiments were performed up to 90 GPa at room temperature using diamond with 200 μm culets and rhenium as the gasket material. The pressure medium is neon, and Au was used to determine the pressure [Fei et al., 2007]. The x-ray wavelength is 0.3344 Å.

3.3 Brillouin and Impulsive Stimulated Light Scattering

The BLS and ISS measurements (the BLS experiments were conducted by Jing Yang) were performed on single crystal Fp8 in a DAC up to 89GPa at room temperature in a 2-5 GPa pressure interval at the Mineral Physics Laboratory of the University of Texas at Austin. To ensure the success of high pressure experiments, the sample platelets with size of $70-100\mu m$ were loaded into the sample chambers of several short symmetrical DAC with various size of diamond culet ($250\mu m, 300\mu m, 350\mu m$). The sample chamber was made of Re gasket. Neon was used as the pressure medium and ruby spheres were loaded along with the sample as a pressure celebrant in the sample chamber.

The BLS system was equipped with a Coherent Verdi V2 laser with a wavelength of 532nm, a Laser Components Single Photon Counting Module (APD; Model: COUNT 10B), and a JRS six-pass tandem Fabry–Pérot interferometer. The laser beam was focused down to approximately $20\mu m$ in diameter at the sample position. The scattered Brillouin signals were collected with a scattering angle of 46.1° which was calibrated using the elastic constants of standard silicate glass, distilled water, and single crystal MgO [Chang et al., 2013 and Yang et al., 2014]. The details of the system setup and the calibration of ISS system have been extensively discussed in Chapter 2.

Based on the following equations:

$$V_{p_{[100]}} = (c_{11}/\rho)^{1/2}$$

$$V_{s_{[100]}} = (c_{44}/\rho)^{1/2}$$

$$V_{p_{[110]}} = [(c_{11} + c_{12} + 2c_{44})/2\rho)^{1/2}$$

$$V_{s_{[110]}} = [(c_{11} - c_{12})/2\rho)^{1/2},$$

the use of the (100) platelet permits determination of the elastic constants (c_{11}, c_{12}, and c_{44}) along principle [100] and [110] axes. ρ is the density and the subscript [uvw] indicates the symmetry family of directions corresponding to the phonon direction of scattering wave [Every, 1980]. At each pressure (up to 89GPa), both compressional and shear acoustic velocities have been measured by ISS and BLS respectively along principle [100] and [110] axes.

CHAPTER 4 RESULTS AND DATA ANALYSES

4.1 Pressure-Volume Equation of State (EoS) and Spin State

High pressure single-crystal X-ray diffraction patterns were collected within a 1-3 GPa pressure interval (Fig. 4.1, data shown in Table. 1). The unit cell volume V was determined based on four sets of diffraction peaks corresponding to (200), (400) (400), and (420) lattice from a single-crystal X-ray pattern. To determine the width of the spin crossover and the occurrence of the high spin and low spin states systematically, we first compared our P-V data with the Equation of State of the end-member MgO as a starting reference at corresponding P-T conditions [Tange et al., 2009]. The measured P-V relation clearly showed an enhanced reduction in volume at the pressure range expected for the spin crossover [Mao et al., 2011]. A third order isothermal Birch-Murnaghan Equation of State was applied to fit the volume data within two pressure ranges for the high spin (to 40 GPa) and low spin (from 60 GPa) phases, yielding $K_{To} = 152.5(2.4)\ \text{GPa}, K_{To}' = 4.1(2), \text{and}\ V_o = 75.5\text{Å}^3$ for high spin state, and $K_{To} = 161.6(7.9)\ \text{GPa}, K_{To}' = 4\ (\text{fixed}), \text{and}\ V_o = 74.1(6)\text{Å}^3$ for low spin state. The derived K_{To} and K_{To}' for the HS and LS states agree with previous reports [Jacobsen et al.,2002; Lin et al., 2005; Speziale et al., 2005].

As the width of the spin transition and the thermal EoS parameters were defined, the fraction of the LS state (n_{LS}) at a given pressure condition (this study was only conducted at room temperature) was obtained (Fig. 4.2). The pressure dependence of n_{LS} can be described by, $n_{LS} = \frac{1}{1+\exp(\Delta G(P,T_0)^*/T_0)}$, where T_0 is the room temperature and

$\Delta G(P, T_0)^*$ is the difference of the Gibbs free energy between the LS and HS states [Tsuchiya et al., 2006; Wentzcovitch et al., 2009]. By performing the least-squares fit on n_{LS} at a given pressure (and room temperature), we can obtain the values of $\Delta G(P, T_0)^*$.

4.2 Bulk Modules and Bulk Sound Velocity

Bulk modulus and bulk sound velocity are modeled by using the obtained EoS (see Sec. 4.1). Wentzcovitch et al. (2009) developed this process. Starting with the volume $V = (1 - n_{LS})V_{HS} + n_{LS}V_{LS}$, where V_{HS} and V_{LS} are the unit cell volume of high-spin and low-spin states at a given pressure (Fig. 4.3(a), plotting as density increases with pressure) the isothermal bulk modulus (Fig4.3 (b)) can be written as

$$\frac{V}{K_T} = n_{LS}\frac{V_{LS}}{K_{LS}} + (1 - n_{LS})\frac{V_{HS}}{K_{HS}} - (V_{LS} - V_{HS})\left(\frac{\partial n_{LS}}{\partial P}\right) .$$

K_{HS} and K_{LS} are the isothermal bulk moduli of high-spin and low-spin states at a given pressure. Assuming the volumetric thermal expansion and the Grüneisen parameter at ambient conditions are the same as MgO, $\alpha_0 = 31.2 \cdot 10{-}6\ K^{-1}$ and $\gamma_0 = 1.524$ [taken from Suzuki, 1975 and Speziale et al., 2001], the bulk sound velocity (Fig 4.3 (c)) was calculated using $V_\phi = \sqrt{\frac{K_T}{\rho}}$.

4.3 Acoustic Wave Velocities

High pressure BLS measurements were performed on the well cleavaged (100) crystallographic plane in [100] and [110] crystallographic directions within two to three degrees of uncertainty. The measurements were performed within 3-5 GPa pressure

intervals up to 89 GPa. Below 20 GPa, the Brillouin spectra showed strong Vp and Vs peaks with high signal-to-noise ratios. Above 20 GPa, the Vp peak was masked by the Vs diamond peak. Figure 4.4 shows the representative Brillouin spectra along [100] and [110]. The BLS measurement was conducted by Jing Yang.

High pressure ISS measurement was performed at the same pressure every time immediately after the BLS measurement in [100] and [110] crystallographic directions up to 89 GPa. Figure 4.5 shows their representative ISS spectra along [100] and [110] (see Appendix IV for Time-Frequency Domain Transformation). The fitted Vp peaks are consistent with those measured from BLS below 20 GPa.

A compressional wave propagates along the [110] axes ($V_{p_{[110]}}$) has a higher velocity than a compressional wave traveling along the [100] axes ($V_{p_{[100]}}$) at a low pressure region (0 to 22GPa). From 22GPa to 89 GPa, $V_{p_{[100]}}$ overruns $V_{p_{[110]}}$. At 38GPa, both $V_{p_{[100]}}$ and $V_{p_{[110]}}$ start to show a softening behavior; the velocities measured are lower than the velocity increase trend with increasing pressure. This abnormal behavior turns back to a normal trend as pressure reaches to 78GPa. For shear wave velocities, $V_{s_{[100]}}$ has a higher velocity than $V_{s_{[110]}}$ at low pressure region. The velocity of $V_{s_{[110]}}$ increases with pressure, and it overruns the velocity of $V_{s_{[100]}}$ at 22 GPa. The velocity of $V_{s_{[100]}}$ does not increase with pressure as others do. Shear wave velocities do not show marked softening behavior at the pressure range where compressional waves are experienced (Fig. 4.6).

The interfacial wave that propagates along the boundary between Fp8 single crystal and pressure medium (neon) has also been detected by ISS. The interfacial wave has no dependence on direction under the experimental condition [Crowhurst et al., 2008]. The interfacial wave velocity can be used to calculate the shear wave velocity. When combined with the compression wave velocity, the elastic constants c_{11}, c_{12} and c_{44} can be derived. However, many assumptions have to be made, like the elastic properties of the pressure medium. Compared with the shear wave velocity measured directly by BLS (Fig. 4.6), the shear wave velocity also has a much smaller measurement uncertainty. Therefore, in this study, we use compressional wave velocity that is measured by ISS and shear wave velocity which is measured by BLS to derive the elastic constants.

4.4 Elastic Constants

The elastic constants, c_{11}, c_{12} and c_{44} (Fig. 4.3(d)), were modeled separately for the high-spin and low-spin states and the mix-spin state.

For pure high-spin and low-spin states, equations of finite strain theory were used [Birch 1978]. The Eulerian finite strain tensor ϵ_{ij} is defined by

$$\epsilon_{ij} = \frac{1}{2}\left(\frac{\partial u_i}{\partial X_j} + \frac{\partial u_j}{\partial X_i}\right) - \frac{1}{2}\sum_k \frac{\partial u_k}{\partial X_i}\frac{\partial u_k}{\partial X_j}$$

where u is a displacement vector and X is the Cartesian coordinates with subscripts [ijk] indicating the three principle axes. We apply hydrostatic pressure in DAC, and the sample undergoes isotropic compressional strain, which

$$\frac{\partial u_i}{\partial X_i} = \frac{\partial u_j}{\partial X_j} = \frac{\partial u_k}{\partial X_k} = \frac{\theta}{3}. \theta = \sum_i \frac{\partial u_i}{\partial X_i} = \frac{\Delta V}{V_0}$$

is the trace of the infinitesimal strain tensor. Therefore, we have

$$\epsilon_{ij} = \epsilon \delta_{ij}$$

with

$$\epsilon = \frac{\theta}{3} - \frac{1}{2}\frac{\theta^2}{9}.$$

An elementary cube of volume

$$V = (dX_i)^3$$

under high pressure has a volume equal to

$$V_0 = \left[dX_i \left(1 - \frac{\partial u_i}{\partial X_i}\right)\right]^3$$

at ambient pressure condition, hence

$$\frac{V}{V_0} = \left(1 - \frac{\partial u_i}{\partial X_i}\right)^3 = \left(1 - \frac{\theta}{3}\right)^3 = \left[\left(1 - \frac{\theta}{3}\right)^2\right]^{3/2},$$

which

$$\frac{V}{V_0} = \left(1 - \frac{2\theta}{3} + \frac{\theta^2}{9}\right)^{3/2} = \left[1 - 2\left(\frac{\theta}{3} - \frac{\theta^2}{18}\right)\right]^{3/2} = (1 - 2\epsilon)^{3/2}.$$

The strain can be defined as

$$f = -\epsilon = \frac{1}{2}[\left(\frac{V}{V_0}\right)^2 - 1].$$

Free energy can be expended in power of f if the energy at no strain is zero and it is quadratic for infinitesimal strain, which

$$A = af^2 + bf^3 + cf^3 + ..., .$$

For the third order expansion,

$$A = af^2 + bf^3$$

and one takes pressure

$$P = -(\frac{\partial A}{\partial V}) \text{ and } K_0 = -\lim_{P\to 0}\left(\frac{PV}{\Delta V}\right)_T$$

from which the following equations can be derived.

$$P = 3K_0 f(1+2f)^{5/2}[1+a_1 f + a_2 f^2]$$
$$a_1 = (3/2)[K_0^{'} - 4]$$
$$a_2 = (3/2)[K_0 K_0^{''} + K_0^{'}(K_0^{'} - 7) + 143/9]$$

where subscript 0 denotes values at zero pressure and prime denotes pressure derivatives. $c_{ijkl}(f) = \int P\, df$ provides the following equation set to calculate the elastic constants.

$$c_{ijkl}(f) = (1+2f)^{7/2}[c_{ijkl}^0 + b_1 f + (1/2)b_2 f^2 + ...] - P\Delta_{ijkl}$$
$$b_1 = 3K_0(c'^0_{ijkl} + \Delta_{ijkl}) - 7c_{ijkl}^0$$
$$b_2 = 9K_0^2 c''^0_{ijkl} + 3K'_0(b_1 + 7c_{ijkl}^0) - 16b_1 - 49c_{ijkl}^0$$
$$\Delta_{ijkl} = -\delta_{ij}\delta_{kl} - \delta_{ik}\delta_{jl} - \delta_{il}\delta_{jk}$$

c^0_{ijkl} represents each elastic constant at room pressure, c'^0_{ijkl} is the pressure derivative of the elastic constant, and c''^0_{ijkl} is the second pressure derivative of the elastic constant. K_0 and K'_0 represent the isothermal bulk modulus at room temperature and its pressure derivative. For Fp8, a cubic material, the following equations,

$$c_{11} \Rightarrow \begin{cases} \Delta_{1111} = -3 \\ b_1 = 3K_0(c'^0_{11} - 3) - 7c^0_{11} \\ b_2 = 9K_0^2 c''^0_{11} + K_0(9K'_0 - 48)(c'^0_{11} - 3) + 63c^0_{11} \end{cases}$$

$$c_{11} = (1+2f)^{7/2}\{c^0_{11} + [3K_0(c'^0_{11} - 3) - 7c^0_{11}]f + 1/2[9K_0^2 c''^0_{11} + K_0(9K'_0 - 48)(c'^0_{11} - 3) + 63c^0_{11}]f^2\} + 3P$$

$$c_{12} \Rightarrow \begin{cases} \Delta_{1122} = -1 \\ b_1 = 3K_0(c'^0_{12} - 1) - 7c^0_{12} \\ b_2 = 9K_0^2 c''^0_{12} + K_0(9K'_0 - 48)(c'^0_{12} - 1) + 63c^0_{12} \end{cases}$$

$$c_{12} = (1+2f)^{7/2}\{c^0_{12} + [3K_0(c'^0_{12} - 1) - 7c^0_{12}]f + 1/2[9K_0^2 c''^0_{12} + K_0(9K'_0 - 48)(c'^0_{12} - 1) + 63c^0_{12}]f^2\} + P$$

$$c_{44} \Rightarrow \begin{cases} \Delta_{2323} = -1 \\ b_1 = 3K_0(c'^0_{44} - 1) - 7c^0_{44} \\ b_2 = 9K_0^2 c''^0_{44} + K_0(9K'_0 - 48)(c'^0_{44} - 1) + 63c^0_{44} \end{cases}$$

$$c_{44} = (1+2f)^{7/2}\{c^0_{44} + [3K_0(c'^0_{44} - 1) - 7c^0_{44}]f + 1/2[9K_0^2 c''^0_{44} + K_0(9K'_0 - 48)(c'^0_{44} - 1) + 63c^0_{44}]f^2\} + P$$

were used to model the high-spin and low-spin state elastic constants [Birch 1978]. Table 5 shows the values of c_{ij} and c_{ij}'.

After we obtained all of the c_{ij} in pure high-spin and low-spin states, the model that was developed by Wu et al (2013) was used to describe the softening behavior of elastic constants in the spin crossover. The mixed spin state in ferropericlase was treated as an ideal solid solution of high-spin and low-spin states. The Gibbs free energy of this mix-spin state was defined as,

$$G(n,\ P,\ T) = nG_{LS}(P,\ T) + (1-n)G_{HS}(P,\ T) + G_{mix},$$

where $n = n(P,T)$ is the low-spin state fraction of irons, G_{LS}, G_{HS}, and G_{mix} are Gibbs free energies of pure low-spin state, high-spin state, and ideal solid solution mixing. Defining the elastic compliances (inverse of the elastic constant,c_{ij}),

$$S^{ij} = -\frac{1}{V}\frac{\partial^2 G}{\partial\sigma_i\,\partial\sigma_j}\bigg|_{P,\,T},$$

where σ_i and σ_j are stress components, V is volume, and P is pressure. Substitute the elastic compliances into the Gibbs free energy equation of the mix-spin state above, for the cubic system, the following equations are derived (for detail, please see Wu et al., 2013 and its supplemental material):

$$S^{11}V = nS^{11}_{LS}V_{LS} + (1-n)S^{11}_{HS}V_{HS} - \frac{1}{9}(V_{LS} - V_{LS})\frac{\partial n}{\partial P}$$

$$S^{12}V = nS^{12}_{LS}V_{LS} + (1-n)S^{12}_{HS}V_{HS} - \frac{1}{9}(V_{LS} - V_{LS})\frac{\partial n}{\partial P}$$

$$S^{44}V = nS^{44}_{LS}V_{LS} + (1-n)S^{44}_{HS}V_{HS}.$$

Using the relationship between elastic constant and elastic complains for cubic material,

$$c_{11} = \frac{S^{11} + S^{12}}{(S^{11})^2 + S^{12}S^{11} - 2(S^{12})^2}$$

$$c_{12} = \frac{-S^{12}}{(S^{11})^2 + S^{12}S^{11} - 2(S^{12})^2}$$

$$c_{44} = \frac{1}{S^{44}}$$

the behavior of the elastic constants of Fp8 in the mix-spin state was modeled.

4.5 Comparison with Previous Studies.

All elastic constants of the HS ferropericlase increase with pressure. They are generally in agreement with previous studies on (Mg,Fe)O [Marquardt et al., 2009b; Jackson et al., 2006]. The spin transition region that we observed is from 40GPa to 60GPa. It is accompanied by reductions in isothermal bulk modules and bulk sound velocity. These observations are consistent with data reported by Marquardt et al. (2009b, BLS measurement of $(Mg_{0.9}Fe_{0.1})O$) and Crowhurst et al. (2008, ISS measurement of $(Mg_{0.94}Fe_{0.06})O$).

The density increase (volume reduction) of the iron ion mostly affects the elastic stiffness tensors, c_{11} and c_{12}, which are directly connected to volume change. In Marquardt et al., (2009b), the sample compressional wave peak was embedded into diamond's shear wave peak at high pressure (above 32GPa in their case). Therefore, they used one of the shear constants ($(c_{11} - c_{12})/2$, from Brillouin scattering) and adiabatic bulk modulus (calculated from X-ray diffraction data) to derive constants c_{11} and c_{12} for a pressure higher than 32GPa. This gave them larger uncertainties in elastic constants c_{11} and c_{12} than in c_{44} (c_{44} can be derived directly from BLS measurement) at high pressure.

In our study, c_{44} does not show marked depression along with the spin transition. This does not agree with Crowhurst et al.,'s (2008) ISS measurement on $(Mg_{0.94}Fe_{0.06})O$,

which was reported to have a pronounced reduction in c_{44}. They used Vs calculated from an interfacial wave and Vp from an ISS measurement to derive elastic constants. This process incorporated many assumptions, including a pressure medium's density and elastic properties, which may have caused difference on c_{44}.

Those consistencies and discrepancies from the comparison of this study with previous studies indicate the advantages of the mineral physics lab at the University of Texas at Austin. High pressure compressional and shear acoustic wave velocities measurements can be performed simultaneously using ISS and BLS techniques. With fewer assumptions and more direct measurements, more reliable elastic properties of the Fp8 under Earth's lower mantle condition have studied in our lab.

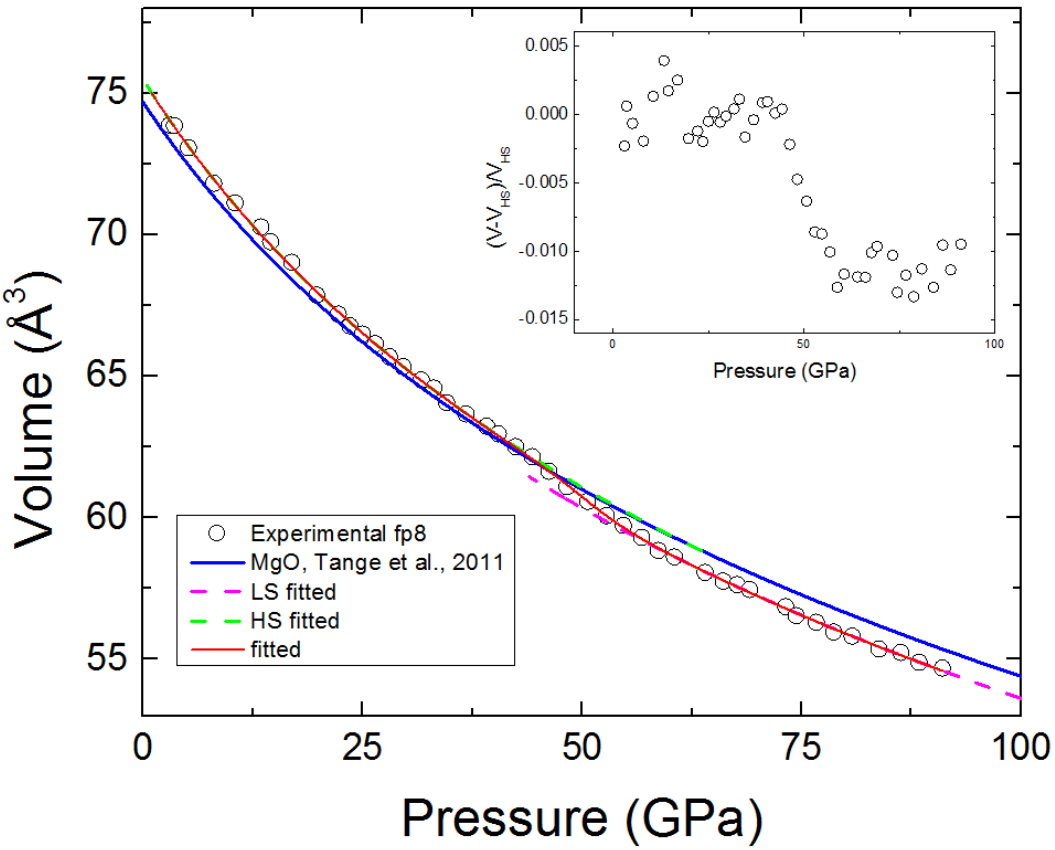

Figure 4.1 Figures by Jing Yang. The isothermal compression curve of $(Mg_{0.92}Fe_{0.08})O$. Green and pink dished lines represent the extrapolation of the HS and LS phases. The blue solid line show results for MgO (Tange et al., 2009) for comparison. The inset in the upper right corner shows the changes of a normalized (to the HS unit cell volume) unit cell volume change with increasing pressure; the deduction is remarkable.

Table 1 Unit cell volume of $(Mg_{0.92}Fe_{0.08})O$ as function of pressure with uncertainties.

P(GPa)	V($\dot{A}^3$)	P(GPa)	V($\dot{A}^3$)	P(GPa)	V($\dot{A}^3$)	P(GPa)	V($\dot{A}^3$)
3.04	73.89±0.13	25.01	66.50±0.04	44.34	62.16±0.12	67.66	57.64±0.11
3.58	73.87±0.03	26.47	66.16±0.01	46.24	61.64±0.02	69.10	57.46±0.15
5.18	73.09±0.04	28.08	65.70±0.04	48.29	61.10±0.09	73.20	56.85±0.09
8.06	71.83±0.12	29.63	65.34±0.01	50.65	60.58±0.01	74.40	56.54±0.15
10.5	71.14±0.08	31.72	64.87±0.03	52.78	59.73±0.10	76.69	56.31±0.04
13.43	70.29±0.26	33.14	64.58±0.09	54.72	59.31±0.06	78.67	55.96±0.18
14.54	69.76±0.11	34.59	64.08±0.13	56.80	58.84±0.12	80.78	55.81±0.01
16.94	69.04±0.17	36.81	63.67±0.03	58.70	58.61±0.02	83.84	55.36±0.13
19.80	67.87±0.13	39.16	63.24±0.08	60.53	58.07±0.04	86.31	55.23±0.14
22.24	67.20±0.09	40.49	62.97±0.09	64.02	57.76±0.04	88.40	54.88±0.02
23.56	66.79±0.15	42.45	62.52±0.05	66.09	57.64±0.11	91.05	54.68±0.15

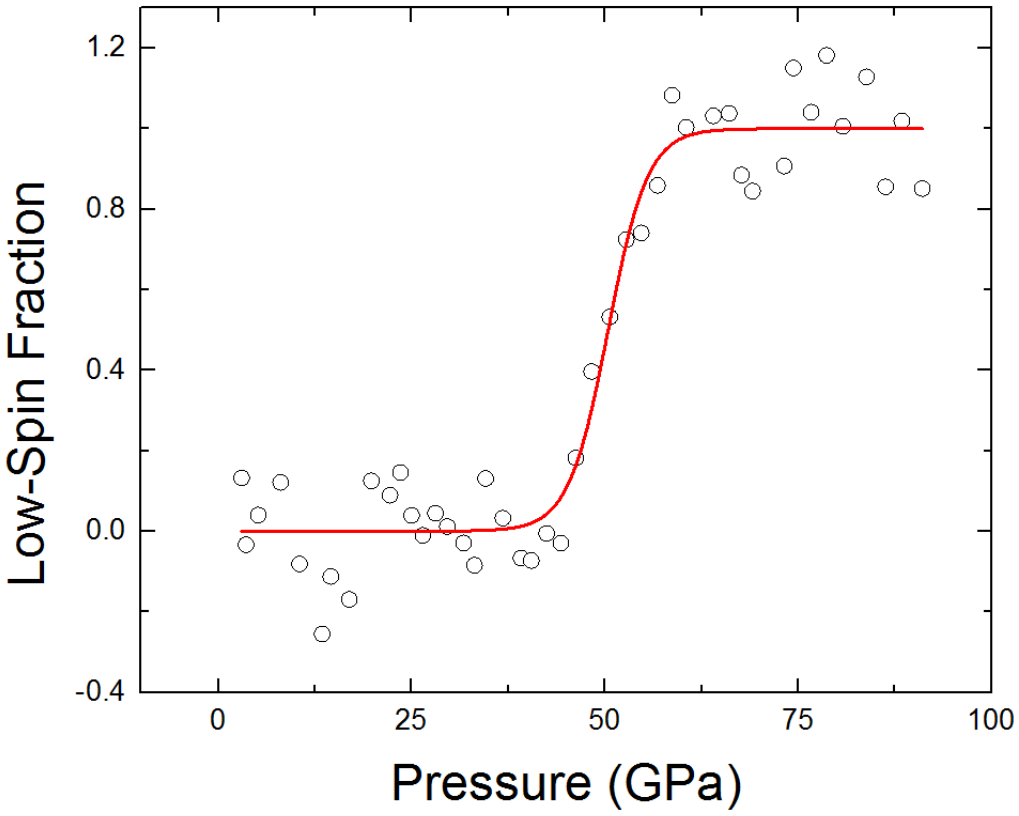

Figure 4.2 Figures by Jing Yang. Derived low spin fractions of Fp8 as a function of pressure compared with the fitting result. Open circles are experimental measurements at room temperature (300 K) and the red line is the fitting result.

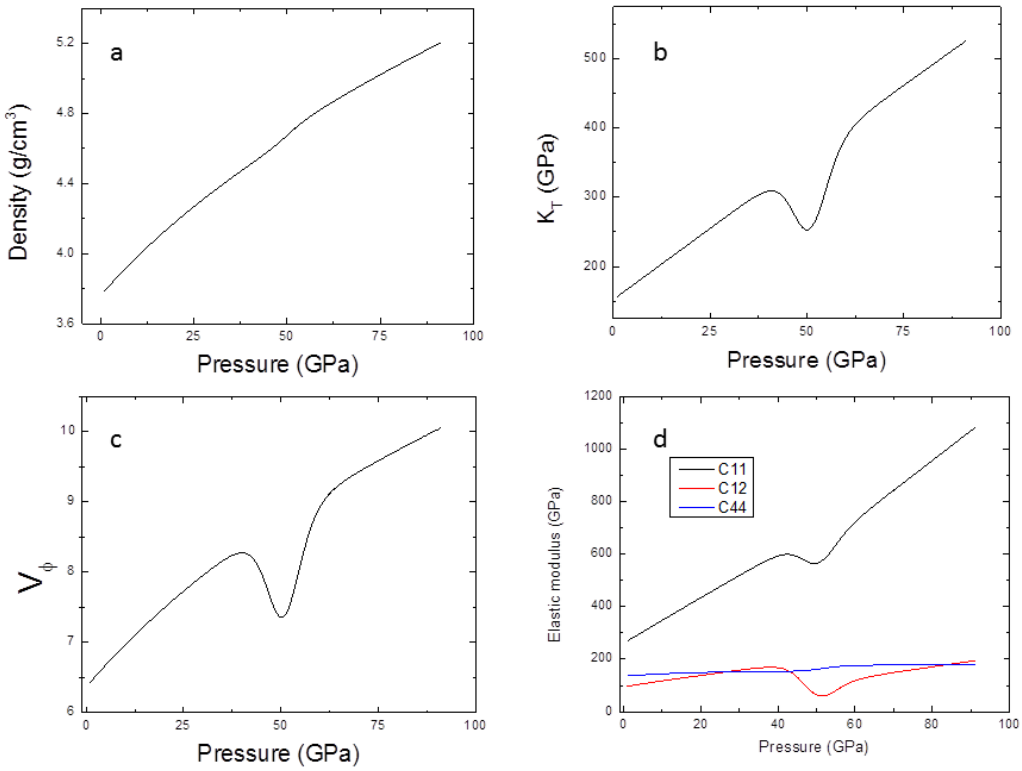

Figure 4.3 Figures by Jing Yang. Density (a), isothermal bulk module (b), and bulk sound velocity(c) of the single crystal $(Mg_{0.92}Fe_{0.08})O$ derived and modeled [Wentzcovitch et al., 2009] from X-ray diffraction measurements. Elastic constants (d) of the single crystal $(Mg_{0.92}Fe_{0.08})O$ were modeled [Wu et al., 2013 and Birch 1978] from BLS and ISS measurements.

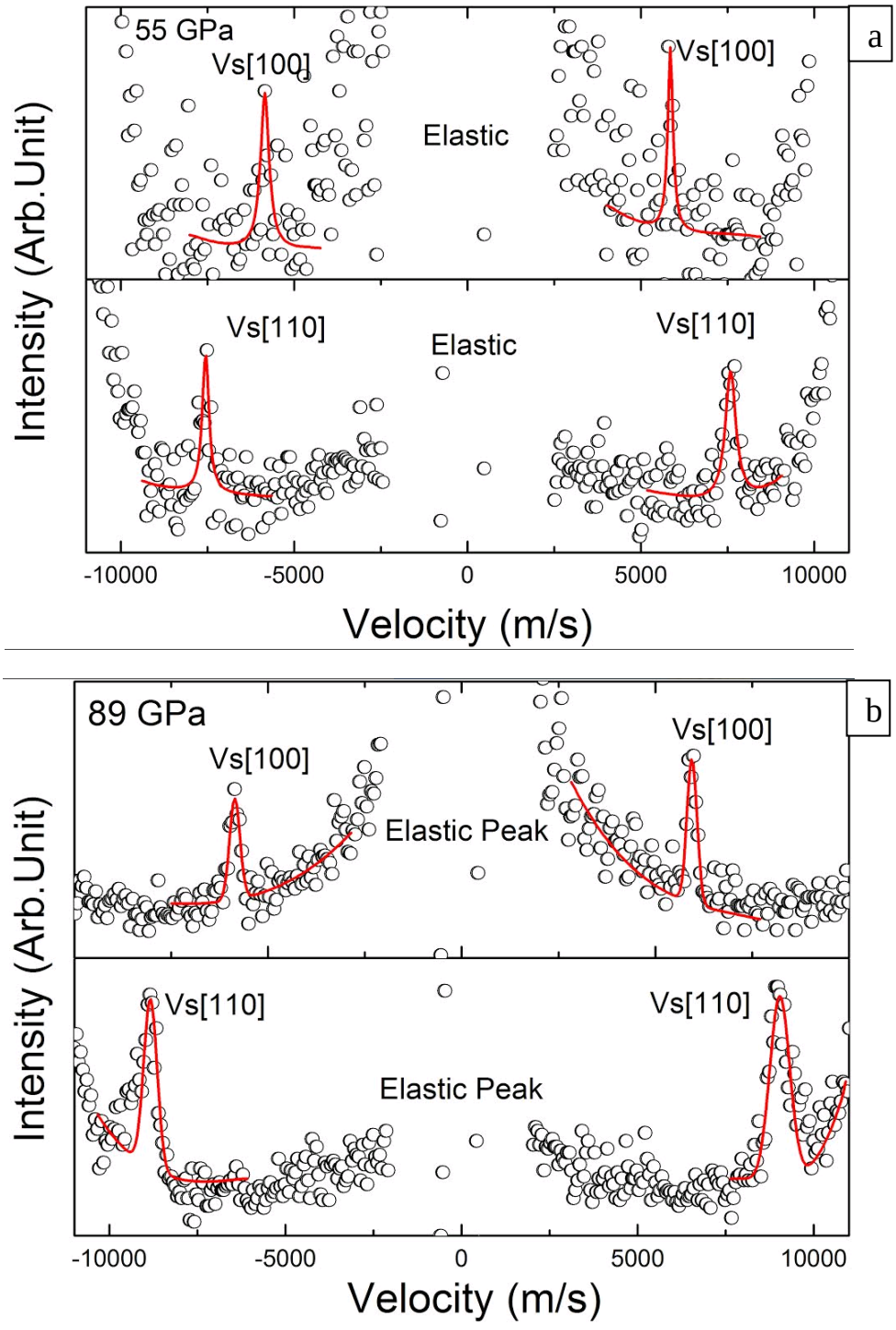

Figure 4.4 Figures by Jing Yang. Representative Brillouin spectra along [100] and [110] at 55GPa (a) and 89GPa (b). Open circles represent the raw data fitted (red solid lines) with Lorentz or Gaussian peak function.

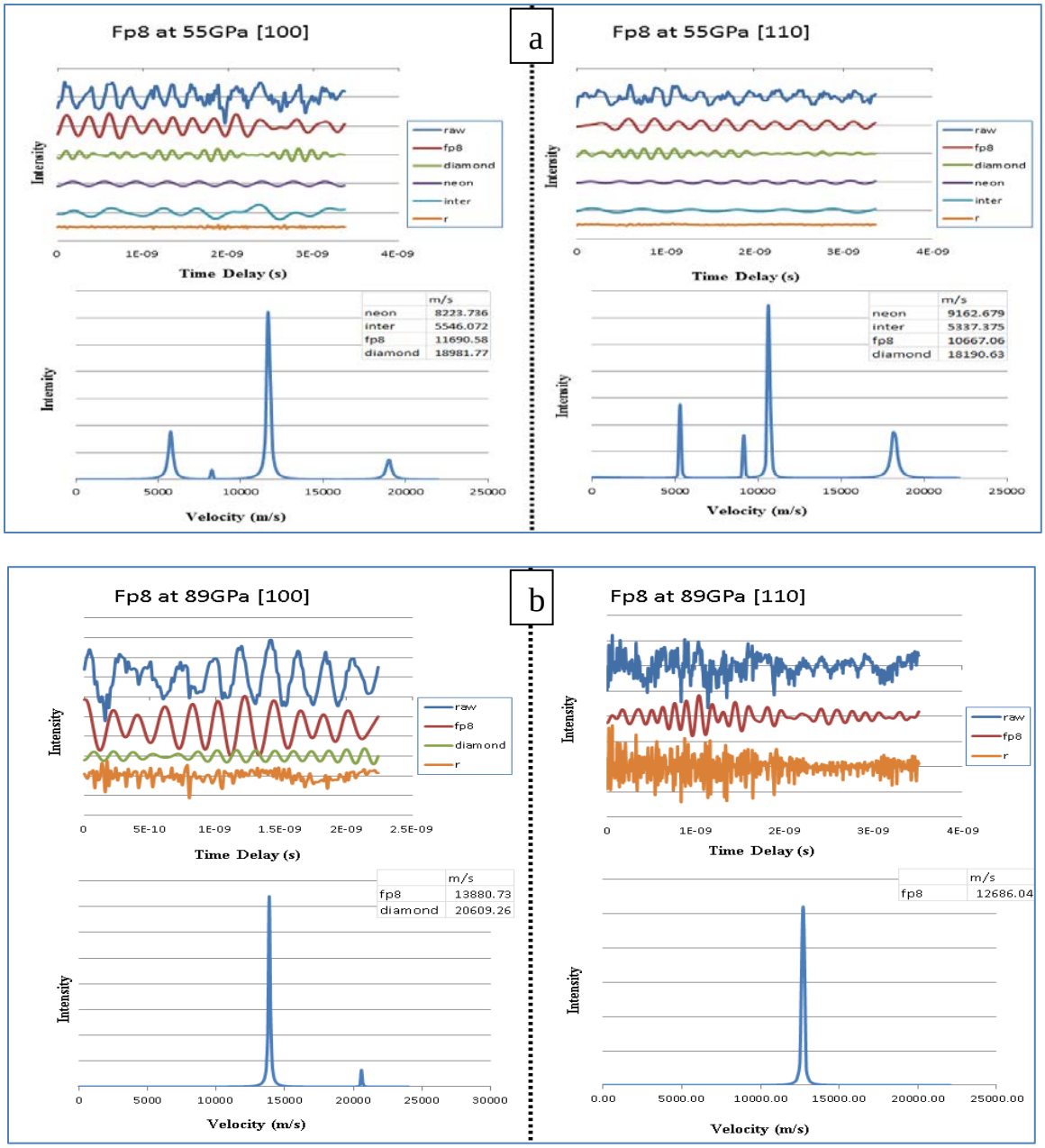

Figure 4.5 Representative ISS spectra along [100] and [110] at 55GPa (a) and 89GPa (b). Top half of a and b consist of original time delay measurements (raw), filtered signals for Fp8 (Vp), Diamond (Vp, not shown at 89GPa [110]), Neon (Vp, not shown at 89GPa), and Interfacial wave velocity (not shown at 89GPa), as well as the residue (r). Bottom half of a and b consist of power spectra of each (Fp8, Diamond, Neon, and Interfacial; from left to right respectively) interested velocity information. The strongest peak in each spectrum is the Vp for Fp8.

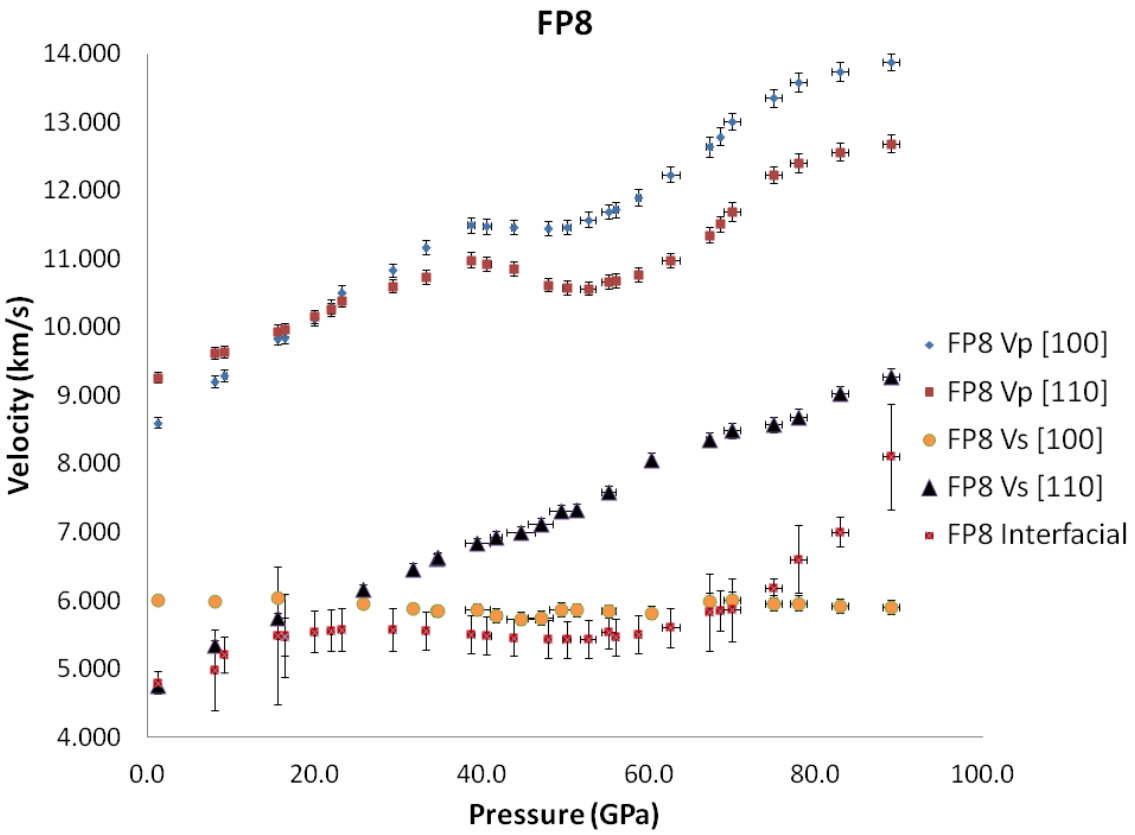

Figure 4.6 Acoustic wave velocities propagate in the (100) plane with increasing pressure for Single crystal Fp8. Solid-filled blue-diamonds and red-squares are compressional wave velocities along [100] and [110] principle axes which were measured by ISS. Filled black-triangles and yellow-circles are BLS measurements of share wave velocities (By Jing Yang). Solid pink-squares are interfacial wave that propagating along the boundary between the Fp8 single crystal and the pressure medium. It has no dependence on direction under the experimental condition [Crowhurst et al., 2008]; compared with the shear wave velocity measured by BLS, the shear wave velocity has much smaller error. Therefore, in this study, we use compressional wave velocities measured by ISS and the shear wave velocities measured by BLS to derive the elastic constants.

Table 2 Shear wave velocities (Vs) data up to 89 GPa, measured by BLS (Measurements were conducted by Jing Yang).

FP8 Vs					
Pressure (GPa)	Error (GPa)	[100] (km/s)	Error (km/s)	[110] (km/s)	Error (km/s)
1.3	0.1	6.010	0.073	4.763	0.058
8.0	0.1	5.993	0.073	5.349	0.065
15.6	0.2	6.046	0.074	5.750	0.070
25.8	0.1	5.962	0.073	6.160	0.075
31.8	0.2	5.885	0.072	6.469	0.079
34.6	0.1	5.846	0.071	6.613	0.081
34.8	0.1	5.847	0.071	6.628	0.081
39.5	1.5	5.867	0.083	6.838	0.083
41.7	0.7	5.782	0.104	6.933	0.085
44.7	1.6	5.740	0.103	7.006	0.086
47.1	1.5	5.741	0.104	7.125	0.087
49.6	1.5	5.865	0.106	7.312	0.089
51.4	0.3	5.865	0.092	7.332	0.090
55.2	0.8	5.847	0.091	7.586	0.093
60.4	0.2	5.824	0.096	8.058	0.098
67.3	0.4	5.998	0.108	8.353	0.102
70.0	1.0	6.017	0.108	8.487	0.104
75.0	1.0	5.966	0.108	8.574	0.105
78.0	1.0	5.966	0.108	8.693	0.106
83.0	1.0	5.923	0.107	9.033	0.110
89.0	1.0	5.902	0.106	9.280	0.113

Table 3 Compression wave velocities (Vp) data up to 89 GPa, measured by ISS.

FP8 Vp					
Pressure (GPa)	Error(GPa)	[100] (km/s)	Error (km/s)	[110] (km/s)	Error (km/s)
1.3	0.1	8.606	0.079	9.267	0.086
8.0	0.1	9.211	0.084	9.620	0.089
9.2	0.2	9.286	0.086	9.645	0.088
15.6	0.2	9.834	0.097	9.945	0.091
16.4	0.2	9.855	0.097	9.967	0.096
20.0	0.1	10.119	0.096	10.153	0.094
22.0	0.2	10.301	0.099	10.258	0.096
23.2	0.1	10.514	0.097	10.396	0.098
29.4	0.1	10.833	0.102	10.601	0.098
33.3	0.1	11.170	0.111	10.734	0.101
38.8	0.5	11.496	0.109	10.985	0.109
40.6	0.5	11.474	0.105	10.925	0.101
43.8	0.2	11.468	0.108	10.853	0.100
48.0	0.1	11.448	0.106	10.621	0.101
50.2	0.5	11.463	0.105	10.581	0.102
52.7	0.9	11.570	0.113	10.569	0.097
55.2	0.8	11.691	0.107	10.667	0.098
56.1	0.3	11.717	0.120	10.679	0.102
58.7	0.3	11.899	0.115	10.772	0.105
62.7	1.1	12.231	0.112	10.980	0.106
67.3	0.4	12.639	0.146	11.349	0.109
68.6	0.1	12.788	0.130	11.516	0.112
70.0	1.0	13.004	0.122	11.696	0.136
75.0	1.0	13.356	0.129	12.227	0.118
78.0	1.0	13.582	0.137	12.406	0.137
83.0	1.0	13.742	0.141	12.564	0.132
89.0	1.0	13.881	0.127	12.686	0.135

Table 4 Best fit of Eulerian finite strain equation parameters of $(Mg_{0.92}Fe_{0.08})O$ based on BLS and ISS results (A). Best fit of Eulerian finite strain equation parameters of $(Mg_{0.9}Fe_{0.1})O$ based on BLS results by Marquardt et al., 2009 (B). Best fit of Eulerian finite strain equation parameters of $(Mg_{0.94}Fe_{0.06})O$ based on BLS results by Jackson et al., 2006 (C).

A	c_{11}^0(GPa)	c_{11}'(GPa)	c_{12}^0(GPa)	c_{12}'(GPa)	c_{44}^0(GPa)	c_{44}'(GPa)
High-spin phase (0-40 GPa)	260.67 ± 13.03	8.896 ± 0.445	95.40 ± 4.67	2.288 ± 0.114	134.75 ± 6.73	1.010 ± 0.051
Low-spin phase (60-89 GPa)	100.69 ± 5.03	9.860 ± 0.493	5.832 ± 0.292	1.910 ± 0.095	50.54 ± 2.53	2.007 ± 0.100

B	c_{11}^0(GPa)	c_{11}'(GPa)	c_{12}^0(GPa)	c_{12}'(GPa)	c_{44}^0(GPa)	c_{44}'(GPa)
High-spin phase (0-45 GPa)	279.5 ± 14	8.71 ± 15	102.2 ± 14	1.47 ±14	142.0 ± 12	0.84 ± 18
Low-spin phase (63-81 GPa)	–	–	–	–	134 ±25	1.2 ±2

C	c_{11}^0(GPa)	c_{11}'(GPa)	c_{12}^0(GPa)	c_{12}'(GPa)	c_{44}^0(GPa)	c_{44}'(GPa)
High-spin phase (0-20 GPa)	284	8.35	103	1.42	147	0.89

CHAPTER 5 GEOPHYSICAL IMPLICATION AND CONCLUSION

This study showed large but smooth decreases in bulk sound velocity and compressional wave velocities. The temperature effect on spin state transition and its consequential effect on the Fp8's elastic properties have not been studied in this project, but further research on this subject will follow. However, even in our room temperature studies, seismic velocities did not show a sudden change at any pressure. Moreover, it has been shown both theoretically and experimentally that the pressure range of spin crossover will broaden as temperature increases [Sturhahn et al., 2005, Tsuchiya et al., 2006, Lin et al., 2007]. Therefore, the spin transition effect on physical properties would have more of a gradual change along the Earth's lower mantle Geotherm rather than a sudden change [Lin and Tsuchiya, 2008]. As a result, the decrease in bulk sound velocity and compressional wave velocity would likely be spread in a large depth range along the Geotherm. The spin transition does not remarkably affect shear wave velocity. According to Marquardt et al.'s (2009a) study on $(Mg_{0.9}Fe_{0.1})O$, bulk (and compressional) and shear wave velocities in parts of the Earth's lower mantle would have a negative correlation on temperature dependence. However, this anti-correlation effect might be obscured if there is no effect on perovskite, as the ferropericlase only composes about 20 vol.% of the lower mantle. Lin et al. (2013) modeled density, bulk modulus (K_S), and bulk sound velocity (V_Φ) of the experimental studies [Brown and Shankland, 1981; Mao et al., 2011a] on $(Mg_{0.75}Fe_{0.25})O$ and the computational study [Wentzcovitch et al., 2009] on $(Mg_{0.8125}Fe_{0.1875})O$ along the Earth's lower mantle geotherm. Although the experimental and computational studies are not in agreement on the spin transition region, both studies

show remarkable softening on bulk modulus and bulk sound velocity in spin crossover. Density also increased 2-4% across the spin transition region. This density contrast may affect the convective behaviors and the temperature profiles of the Earth's mantle [Bower et al., 2009].

In this study, both BLS and ISS were used to measure the elastic constants of $(Mg_{0.92}Fe_{0.08})O$ at HS state, LS state, and through the pressure-induced HS-to-LS transition. There was a large pressure range which c_{11} and c_{12} exhibited a softening, while c_{44} did not register such an anomaly. The pressure derivative of elastic constants in LS state was lower than in HS state for c_{11} and c_{44}, but it showed the opposite for c_{12}. The shear wave anisotropy increased with increasing pressure. The compressional wave anisotropy also increased with increasing pressure, but the increase rate slowed down at higher pressure. Compared with previously published data of ferropericlase with close compositions ([Marquardt et al., 2009b], BLS measurement of $(Mg_{0.9}Fe_{0.1})O$ and [Crowhurst et al., 2008], ISS measurement of $(Mg_{0.94}Fe_{0.06})O$), this study provides more reliable elastic properties information by taking the advantage of simultaneous measurements on BLS and ISS. Moreover, the elastic constants of ferropericlase at the spin transition region and the LS state have been well studied in this thesis; these subjects have not been well documented in the literatures.

In this study, the post spin transition relaxation behavior was also observed (Fig. 5.1). This shows that a typical treatment of spin transition as a spontaneous strain effect is not sufficient. A structural feature, other than strain has to be taken into account [Carpenter M.A. and Salje E. K.H., 1998]. The observed relaxation behavior might be

explained by consider the susceptibility of the structural feature and the strength of coupling between the structural feature and the volume stain [Zhang et al., 2012]. Further studies are needed to use this Landau Theory like model to fully explain this relaxation behavior.

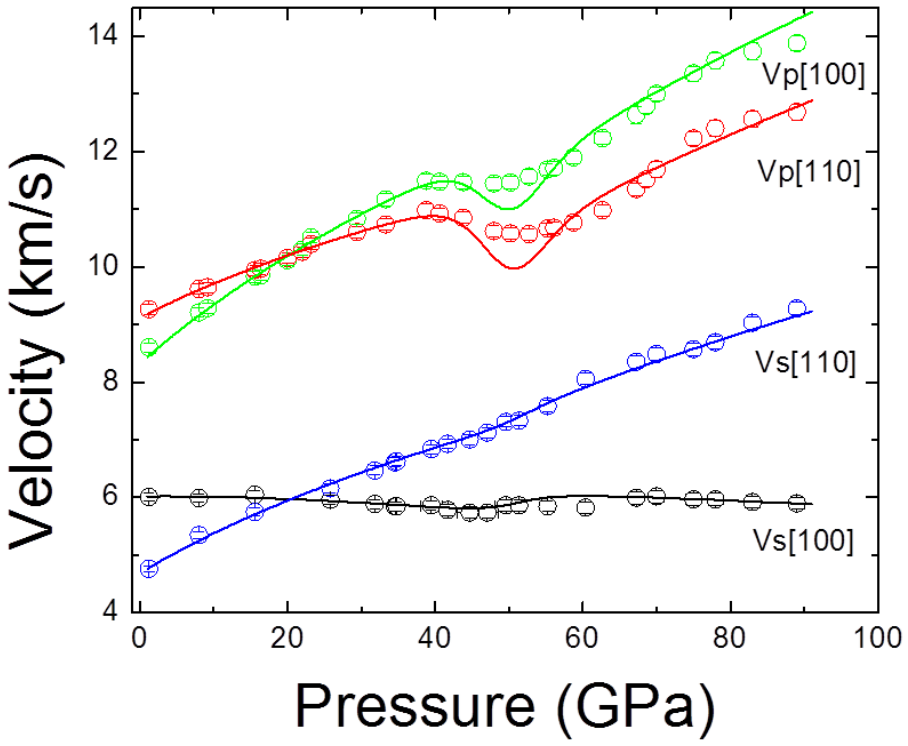

Figure 5.1 Open circles are Vp and Vs measurements from ISS and BLS. Solid curves are predicted velocity profiles by using finite strain theory with the assumption that the spin transition only has a spontaneous strain effect on the materials' elastic behavior. The miss fit (especially within and right after the spin-transition region) between the measured and the predicted velocity profiles indicate that the susceptibility of the structural feature and the strength of coupling between the structural feature and the volume stain have to be taken into account to better explain the softening in the spin transition region and the post spin transition relaxation behavior.

Appendix

Appendix I Thermal Diffusivity and Surface Wave Velocity Measurement and Heterodyning Detection Technique

A. Thermal Diffusivity Measurement

As the discussion in Sec. 2.2, the spatially periodic distribution of temperature remains after the acoustic wave has been fully damped. This is an exponential decay thermal grating which can be represented by the following equation, $R = 1/\tau = \frac{4\pi^2 D}{d^2}$. R and τ are the periodic temperature distribution relaxation rate constant and time. D is the thermal diffusivity (thermal conductivity divided by unit volume heat capacity) and d is the grading spacing which depends on the excitation beams wavelength and the angle between two beams. The one-dimensional thermal diffusion can be obtained with variation of R and d (angle between two excitation beams). The values of D along different crystallographic directions serves to obtain all elements of the crystal thermal diffusivity tensor (a second order tensor) [Abramson et al., 1999].

Followings are part of literatures that one may make use of if interested in doing thermal properties study on ISS.

Abramson, E.H., J.M. Brown, and L.J. Slutsky, (1999) Applications of impulsive stimulated scattering in the earth and planetary sciences, Ann. Rev. Phys. Chem., 50, 279-313

Landa, M., Verstraeten, B., Sermeus, J., Salenbien, R., Sedlak, P., Seiner, H., Glorieux, C., (2011) Thermomechanical properties of single crystals evaluated by impulsive stimulated thermal scattering technique, J. Phys.: Conf. Ser 278 012023

Kading, O. W., Skurk, H., Maznev, A. A., and Matthias, E., "Transient thermal gratings at surfaces for thermal characterization of bulk materials and thin films," Appl. Phys. A 61(3), 253-261(1995)10.1007/BF01538190

Johnson, A.J., Maznev, A.A., Nelson, A.K., Bulsara, T.M., Fitzgerald, A.E., Harman, C.T., Calawa, S., Vineis, J.C., Turner, G., (2012) Phsae-controlled, heterodyne laser-induced transient grant grating measurements of thermal transport properties in opaque material, J. Appl. Phys. 111, 023503

B. Surface Wave Velocity Measurement

Both compressional and shear wave velocities of a crystal can be derived from its surface or interfacial waves. The density of the crystal and the elastic properties of the contacting

materials (oriented metal, optically opaque material, or pressure medium) at different pressure are needed for the calculation.

Followings are part of literatures that one may make use of if interested in doing surface wave velocity study on ISS.

Abramson, E.H., J.M. Brown, and L.J. Slutsky, (1999) Applications of impulsive stimulated scattering in the earth and planetary sciences, Ann. Rev. Phys. Chem., 50, 279-313

Brown, M.J., Abramson, H.E., Angel, J.R., (2006) Triclinic elastic constants for low albite, Phys Chem Minerals 33: 256-365

Crowhurst, C.J., Abramson, H.E., Slutsky, J.L., Brown, M.J., Zaug, M.J., Harrell, D.H., (2001) Surface acoustic waves in the diamond anvil cell: An application of impulsive stimulated light scattering, Physical Review B, Vol. 64, 100103(R)

Landa, M., Verstraeten, B., Sermeus, J., Salenbien, R., Sedlak, P., Seiner, H., Glorieux, C., (2011) Thermomechanical properties of single crystals evaluated by impulsive stimulated thermal scattering technique, J. Phys.: Conf. Ser 278 012023

Maznev, A.A., Every, G.A., (1997) Time-Domain Dynamic Surface Response Of An Anisotropic Elastic Solid To An Impulsive Line Force, Int. J. Engng Sci. Vol 35 No. 4 pp. 321-327

Zhao, L., Baer, J.B., Yamaguchi, M., Than, T.H., Yarmoff, J., (2001) Impulsive Stimulated Scattering Of Surface Acoustic Waves On Metal And Semiconductor Crystal Surface, J. Chem. Phys. 114, 4989

C. Heterodyning Detection

In current ISS system setup (see Sec. 2.3), the intensity of diffracted probe beam can be expressed as $I = I_p = (A_{th} - \sum_i A_{iac}\cos(2\pi f_i))^2$. A_{th} is the amplitude from thermal grating contribution. A_{iac} are the amplitude of acoustic gratings (Fp8, Neon, Diamond, Interfacial, etc.). In optic heterodyning detection setup, the signal intensity $I = (I_P I_R)^{1/2}$. I_P and I_R are the intensities of the reference beam and the weakly diffracted probe. In this approach, one can get considerable increase in the signal intensity and improve in optic alignment easiness [Abramson et al., 1999].

Followings are part of literatures that one may make use of if interested in upgrading the detection technique in ISS.

Abramson, E.H., J.M. Brown, and L.J. Slutsky, (1999) Applications of impulsive stimulated scattering in the earth and planetary sciences, Ann. Rev. Phys. Chem., 50, 279-313

Johnson, A.J., Maznev, A.A., Nelson, A.K., Bulsara, T.M., Fitzgerald, A.E., Harman, C.T., Calawa, S., Vineis, J.C., Turner, G., (2012) Phsae-controlled, heterodyne laser-induced transient grant grating measurements of thermal transport properties in opaque material, J. Appl. Phys. 111, 023503

Landa, M., Verstraeten, B., Sermeus, J., Salenbien, R., Sedlak, P., Seiner, H., Glorieux, C., (2011) Thermomechanical properties of single crystals evaluated by impulsive stimulated thermal scattering technique, J. Phys.: Conf. Ser 278 012023

Maznev, A.A., and Nelson, K.A., (1998) Optical heterodyne detection of leaser-induced gratings, Optics Letters, Vol. 23, No. 16

Appendix II Instrumentation of Impulsive Stimulated Light Scattering System in Mineral Physics Lab at The University of Texas at Austin

A. Laser:

Coherent Talisker Ultra (532-08) Industrial Picosecond Laser System with two frequency (1064nm and/or 532nm) modes/outputs (see Table A.1 for the power range).

Typical operation setup is 200kHz, 532nm Mode, 141.1^{o}C LBO temperature and 9% Attenuation with Divided Mode (with the divisor of 10).

The maximum IR power output for DAC is 50mW for IR lenses of 25 cm FL. The focus spot size is about 40-50 ums for the IR beams and 30-40 um for the 532 nm beam (on Pt foil).

Table A.1: Laser Power Range (200 kHz, 9% Attenuation, Divided Mode)

Laser Power Range (200kHz, 9% Attenuation, Divided Mode)		
Mode/Output	1064nm output (W)	532nm output (W)
1064nm mode	0.016-14.11	0.006-1.877
532nm mode	0.010-6.474	0.006-6.063

The output power can also be adjusted manually by rotate the wave plates for each Laser output.

Table A. 2: Laser Power Range (wave plate)

Laser Power Range (wave plate)		
Mode/Output	Minima	Maxima
1064nm output	-3^{o}	42^{o}
532nm output	0^{o}	45^{o}

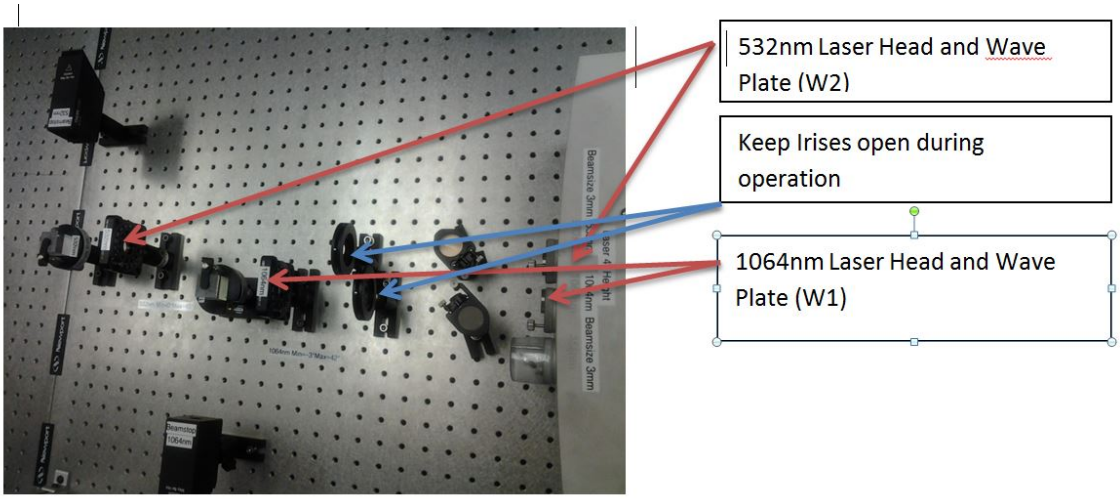

Figure A.1: Laser Head and Wave Plates

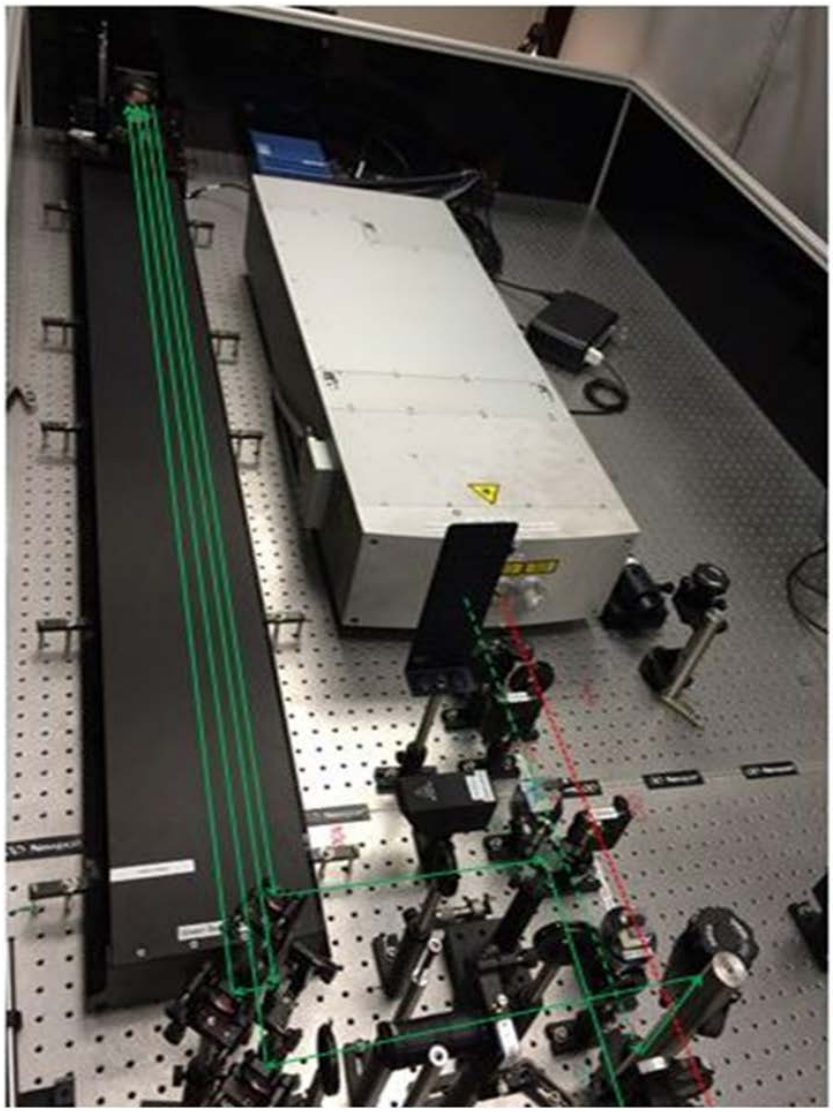

Figure A.2. The Translation Stage and the 4 delay paths for 532nm probe Laser. The length of the translation stage is about 5 ft. long. These equivalents to 20ns delay for the probe beam.

B. Translation Stage (Fig. A.2):

AEROTECH PRO225 (5 ft long) Mechanical-Bearing Ball-Screw Linear Stage coupled with Soloist CP Controller and PWM Digital Drive. The translation stage has been integrated to the ISS Measurement LabView VI; it can also be controlled by Soloist Motion Composer from the computer (Fig. A.3)

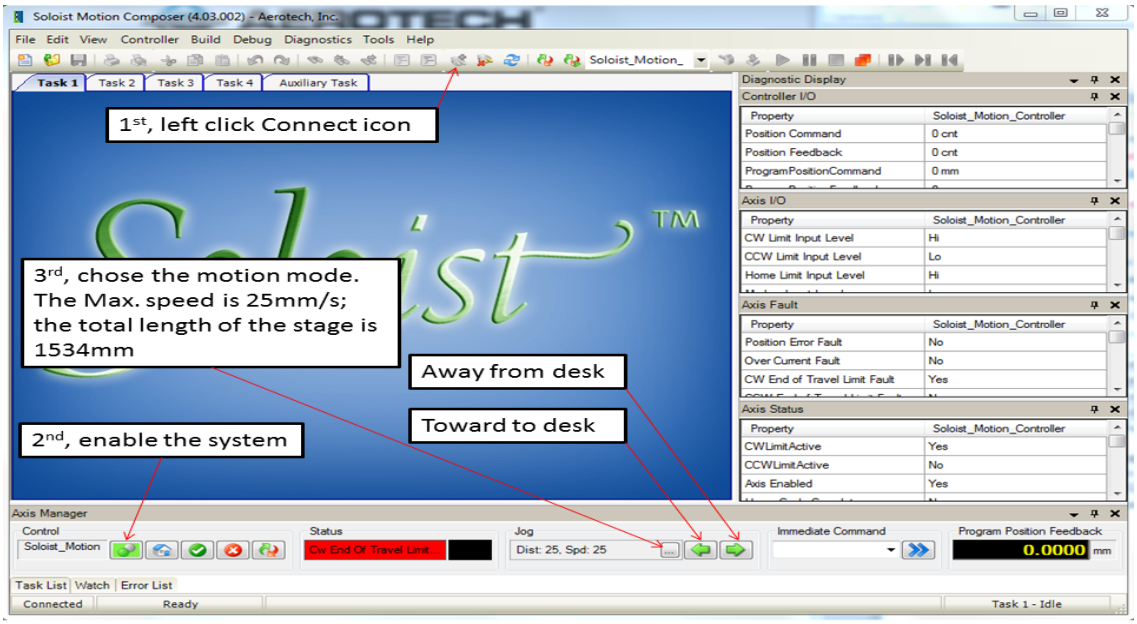

Figure A.3: Control the translation stage via soloist motion composer

C. Lock-In Amplifier:

SR830 DSP Lock-In Amplifier. It has also been integrated to the ISS measurement LabView VI; It can also be controlled from the front panel.

D. Photodetector:

Thorlabs DET36A Photodetector.
Dark current: 0.35na
Wavelength range: 350-1100nm
Raise time: 14ns

Appendix III Product Information of HOYA HA-50 Heat Absorbing Filter

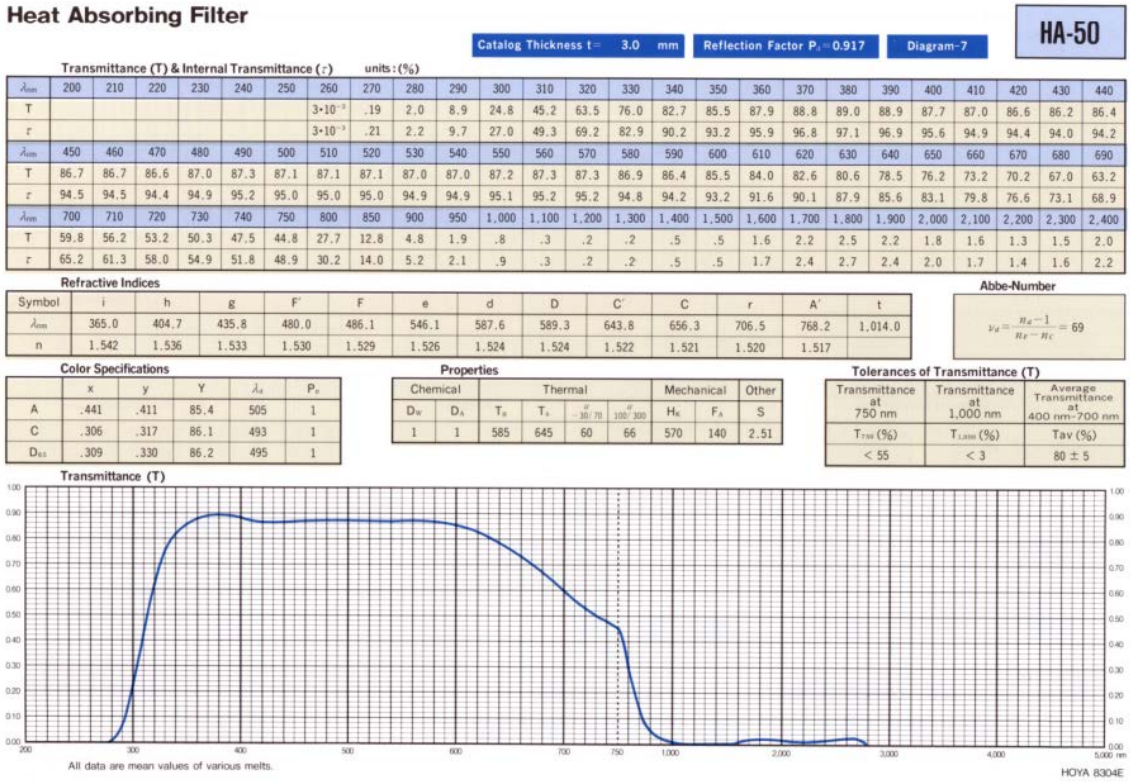

Heat Absorbing Filter

HA-50

Catalog Thickness t = 3.0 mm | Reflection Factor P_d = 0.917 | Diagram-7

Transmittance (T) & Internal Transmittance (τ) units : (%)

λ_{nm}	200	210	220	230	240	250	260	270	280	290	300	310	320	330	340	350	360	370	380	390	400	410	420	430	440
T							$3\cdot10^{-3}$	.19	2.0	8.9	24.8	45.2	63.5	76.0	82.7	85.5	87.9	88.8	89.0	88.9	87.7	87.0	86.6	86.2	86.4
τ							$3\cdot10^{-3}$	.21	2.2	9.7	27.0	49.3	69.2	82.9	90.2	93.2	95.9	96.8	97.1	96.9	95.6	94.9	94.4	94.0	94.2
λ_{nm}	450	460	470	480	490	500	510	520	530	540	550	560	570	580	590	600	610	620	630	640	650	660	670	680	690
T	86.7	86.7	86.6	87.0	87.3	87.1	87.1	87.1	87.0	87.0	87.2	87.3	87.3	86.9	86.4	85.5	84.0	82.6	80.6	78.5	76.2	73.2	70.2	67.0	63.2
τ	94.5	94.5	94.4	94.9	95.2	95.0	95.0	95.0	94.9	94.9	95.1	95.2	95.2	94.8	94.2	93.2	91.6	90.1	87.9	85.6	83.1	79.8	76.6	73.1	68.9
λ_{nm}	700	710	720	730	740	750	800	850	900	950	1,000	1,100	1,200	1,300	1,400	1,500	1,600	1,700	1,800	1,900	2,000	2,100	2,200	2,300	2,400
T	59.8	56.2	53.2	50.3	47.5	44.8	27.7	12.8	4.8	1.9	.8	.3	.2	.2	.5	.5	1.6	2.2	2.5	2.2	1.8	1.6	1.3	1.5	2.0
τ	65.2	61.3	58.0	54.9	51.8	48.9	30.2	14.0	5.2	2.1	.9	.3	.2	.2	.5	.5	1.7	2.4	2.7	2.4	2.0	1.7	1.4	1.6	2.2

Refractive Indices

Symbol	i	h	g	F'	F	e	d	D	C'	C	r	A'	t
λ_{nm}	365.0	404.7	435.8	480.0	486.1	546.1	587.6	589.3	643.8	656.3	706.5	768.2	1,014.0
n	1.542	1.536	1.533	1.530	1.529	1.526	1.524	1.524	1.522	1.521	1.520	1.517	

Abbe-Number

$$\nu_d = \frac{n_d - 1}{n_F - n_C} = 69$$

Color Specifications

	x	y	Y	λ_d	P_e
A	.441	.411	85.4	505	1
C	.306	.317	86.1	493	1
D_{65}	.309	.330	86.2	495	1

Properties

Chemical		Thermal				Mechanical		Other
D_W	D_A	T_g	T_s	$\alpha_{-30/70}$	$\alpha_{100/300}$	H_K	F_A	S
1	1	585	645	60	66	570	140	2.51

Tolerances of Transmittance (T)

Transmittance at 750 nm	Transmittance at 1,000 nm	Average Transmittance at 400 nm–700 nm
T_{750} (%)	$T_{1,000}$ (%)	Tav (%)
< 55	< 3	80 ± 5

Transmittance (T)

All data are mean values of various melts.

HOYA 8304E

Provided by the manufactory, Hoya Corporation USA Optics Division.
http://www.hoyaoptics.com/pdf/HA50.pdf

Appendix IV Time-Frequency Domain Transformation

Burg method is used to do the time-frequency domain transformation. The burg method is an autoregressive model. It specifies that the output variable depends on its own previous values as well as its predicted future values. Therefore, the burg method can minimize the forward and backward prediction errors in the least squares sense, and it always produces a stable model. MatLab and Origin are used to implement the process.

Following, I use the ISS measurement on Fp8 [100] at 1.5 GPa to demonstrate the process of time-frequency domain transformation and filtering for each individual velocity information.

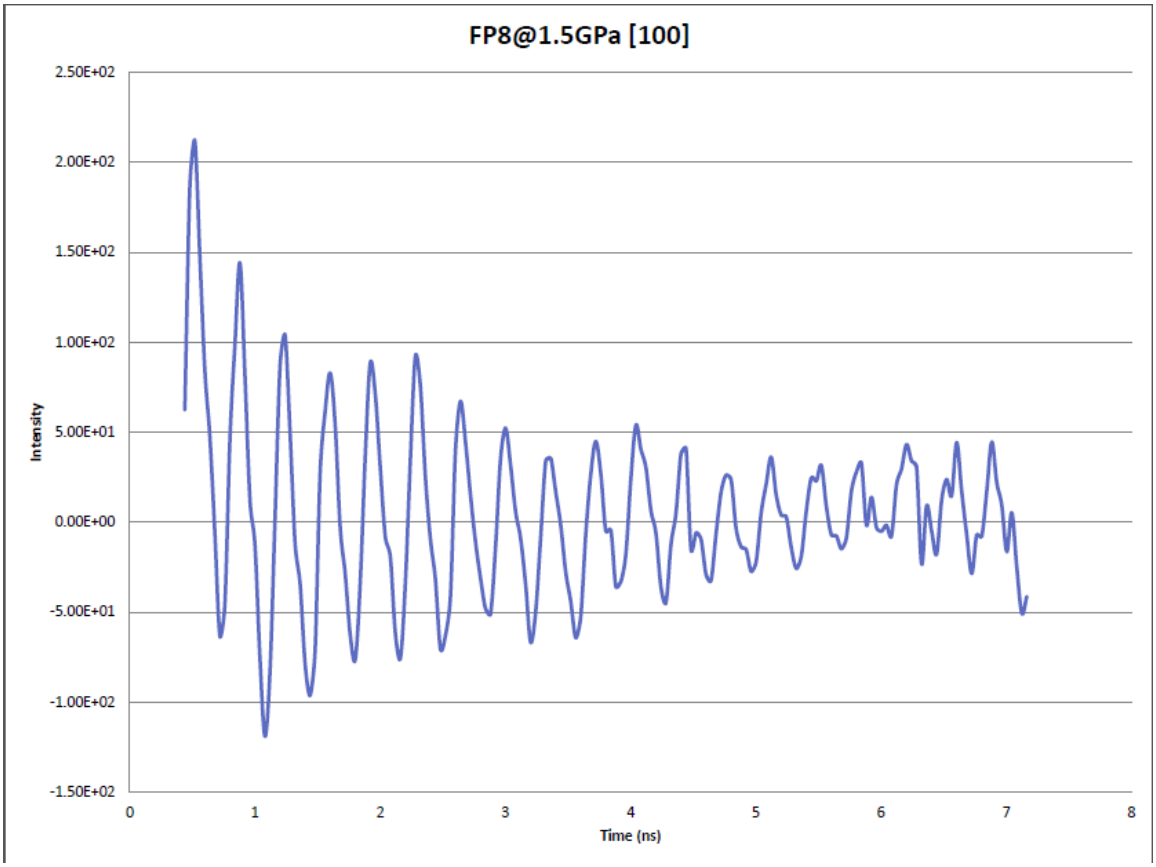

Figure A.4 This is the original measurement on Fp8 [100] at 1.5GPa. The intensity of the diffracted probe beam modulated as function of time delay.

The first step is to remove the background noise and mean value of the measurement. One can use polynomial fit to get the background, remove it from the original measurement with the mean value. I use MatLab to implement this.

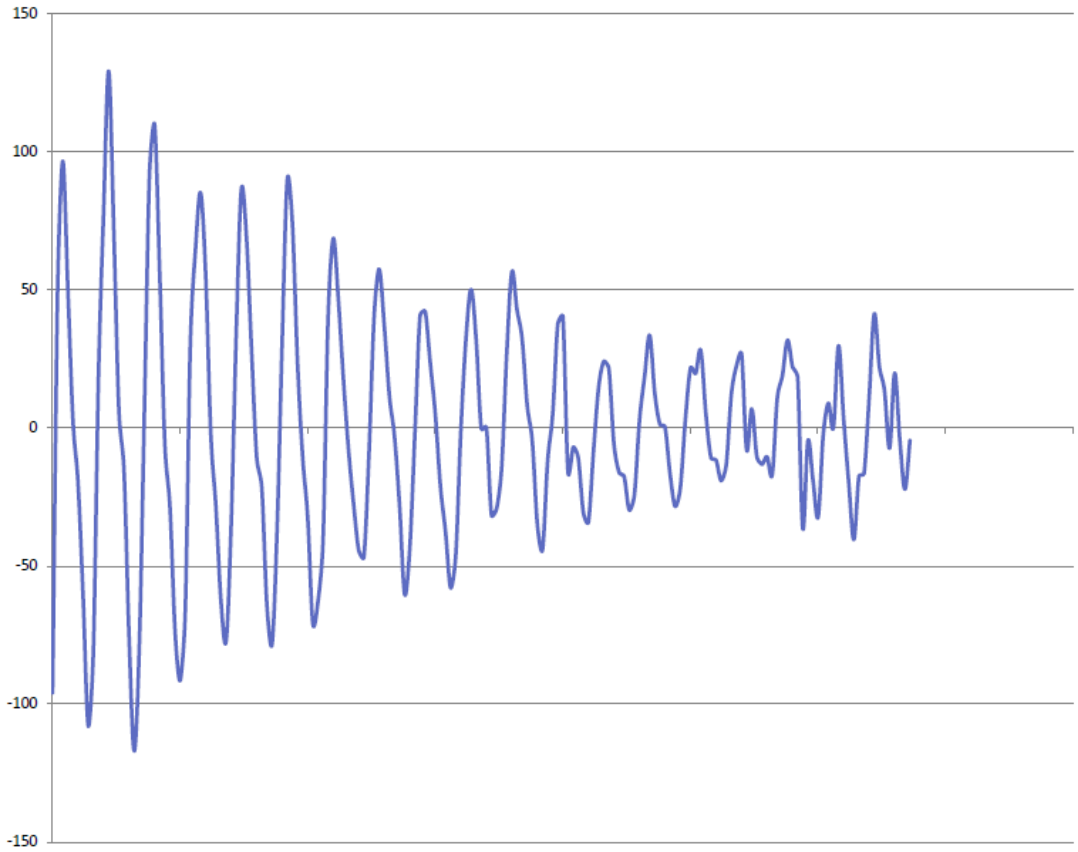

Figure A.5 Background noise and mean value have been removed from the original measurement.

The 'sptool', a built-in tool box in MatLab can be used to do the time-frequency domain transformation (lower-left part of Fig. A.6). The 'FFT Filter' in Origin can be used to build the filter (right part of Fig. A.6). The first velocity information extracted is the compressional wave velocity of Fp8.

Build the filter for FP8 Vp

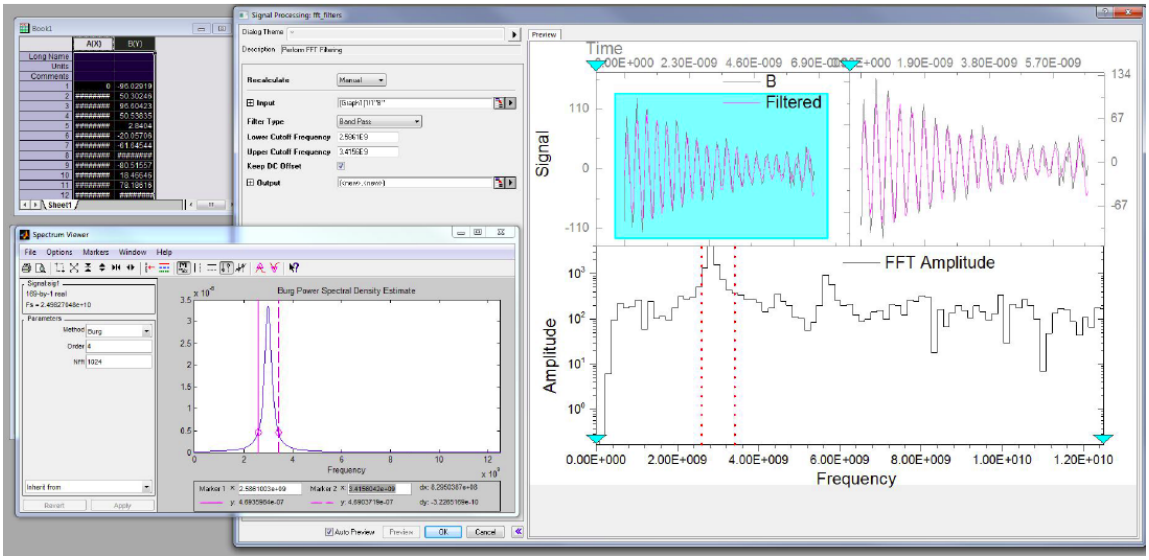

Figure A.6 Time-frequency domain transformation and the filter for Fp8

One can use the residuals (Figure A.7, with the Fp8 Vp information removed, a band block filter) to repeating the steps above to get the velocity information of Diamond (Figure A.8), interfacial wave(Figure A.9), and Neon(Figure A.10).

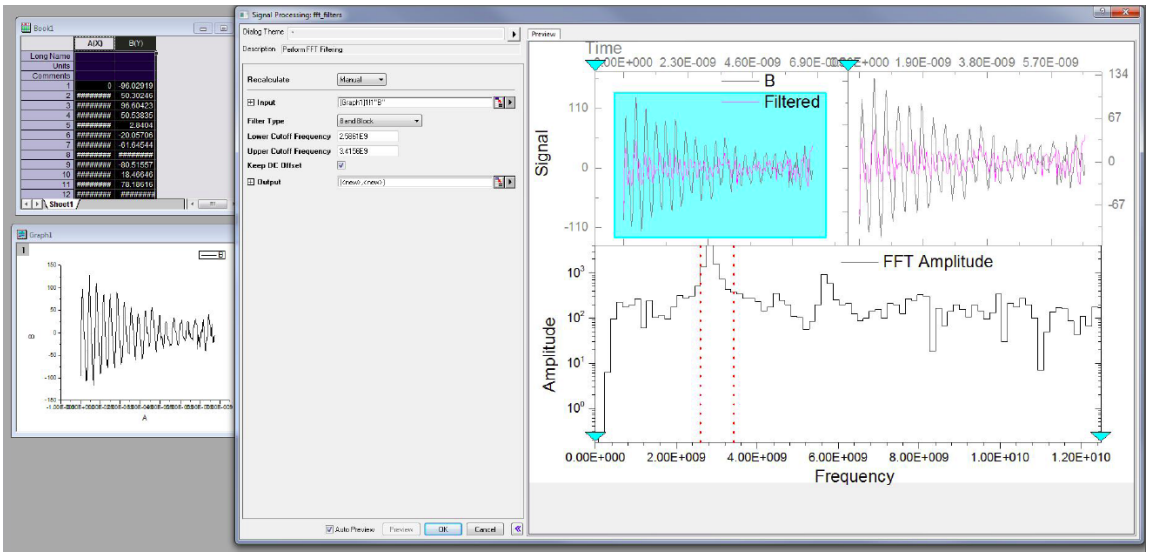

Figure A.7 Residuals, with the Fp8 Vp information removed use a band block filter

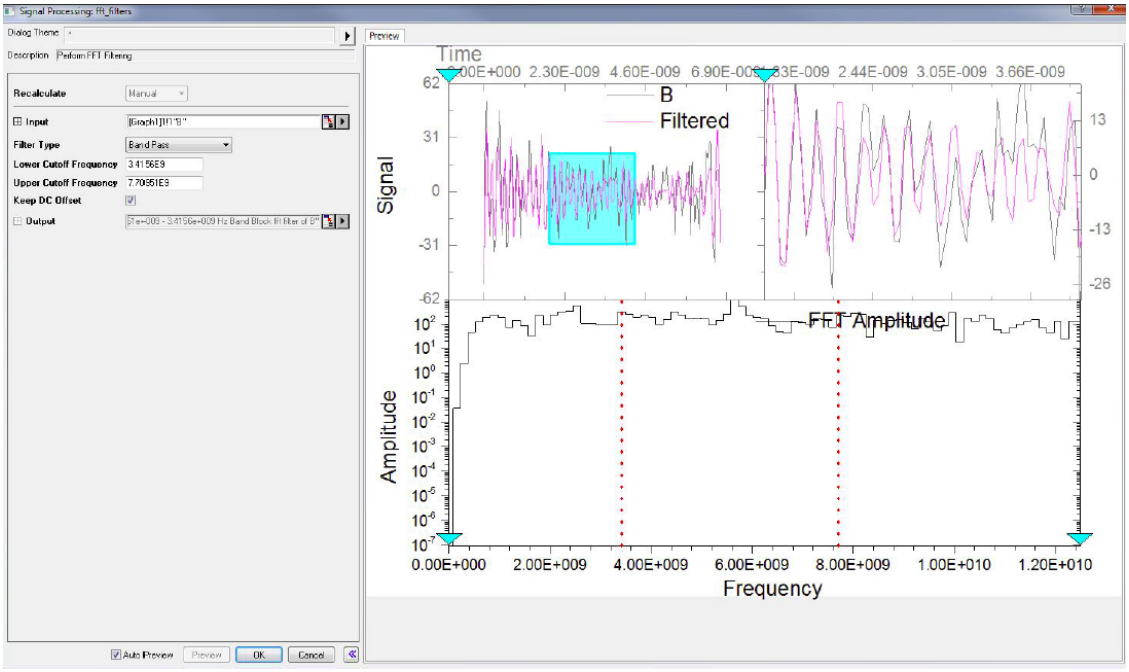

Figure A.8 Filter for Diamond

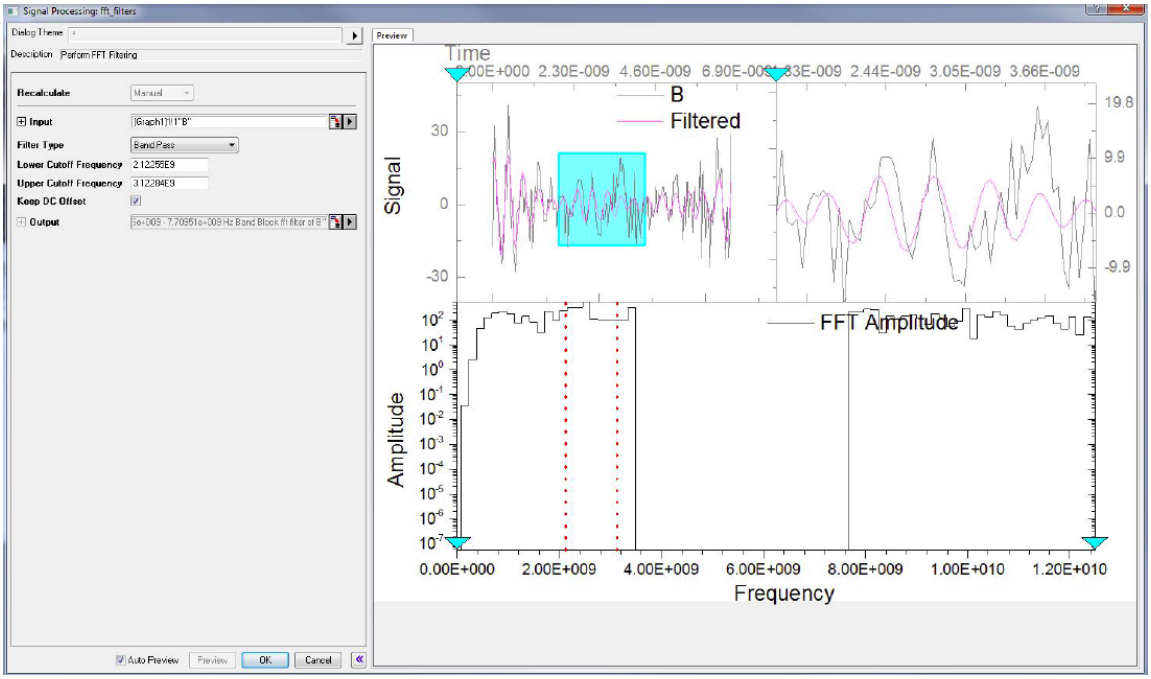

Figure A.9 Filter for Interfacial wave

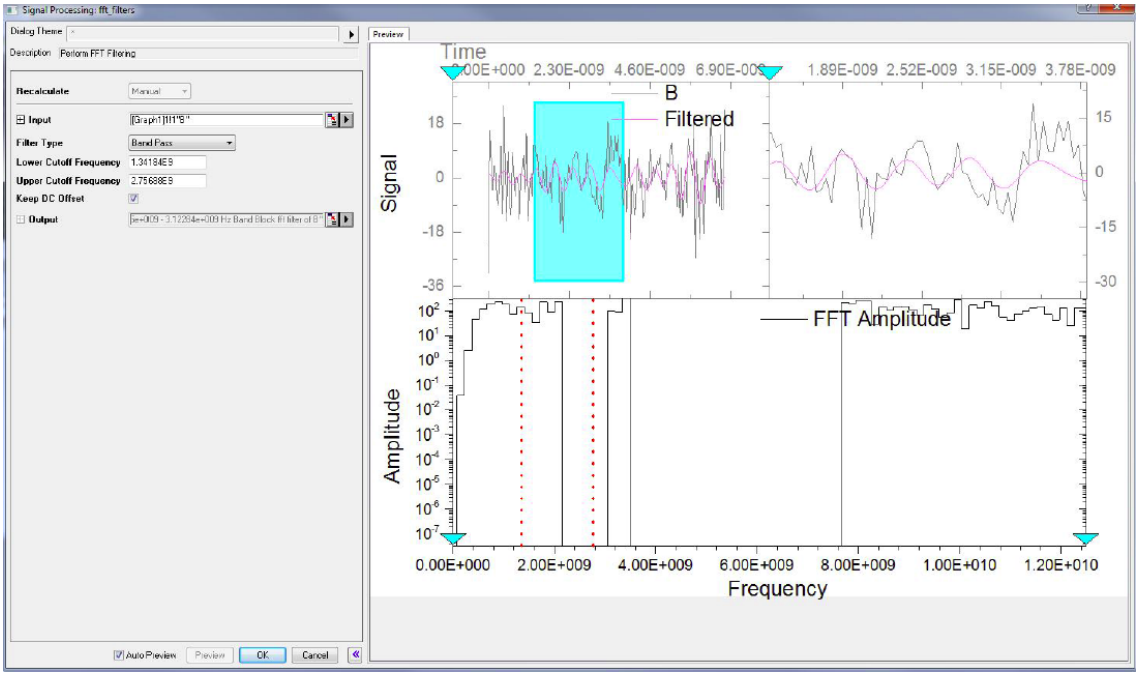

Figure A.10 Filter for Neon

After get all the velocity information (Fp8, Diamond, Neon, and Interfacial), total residual (Figure A.11) with very minimum intensity level was left out.

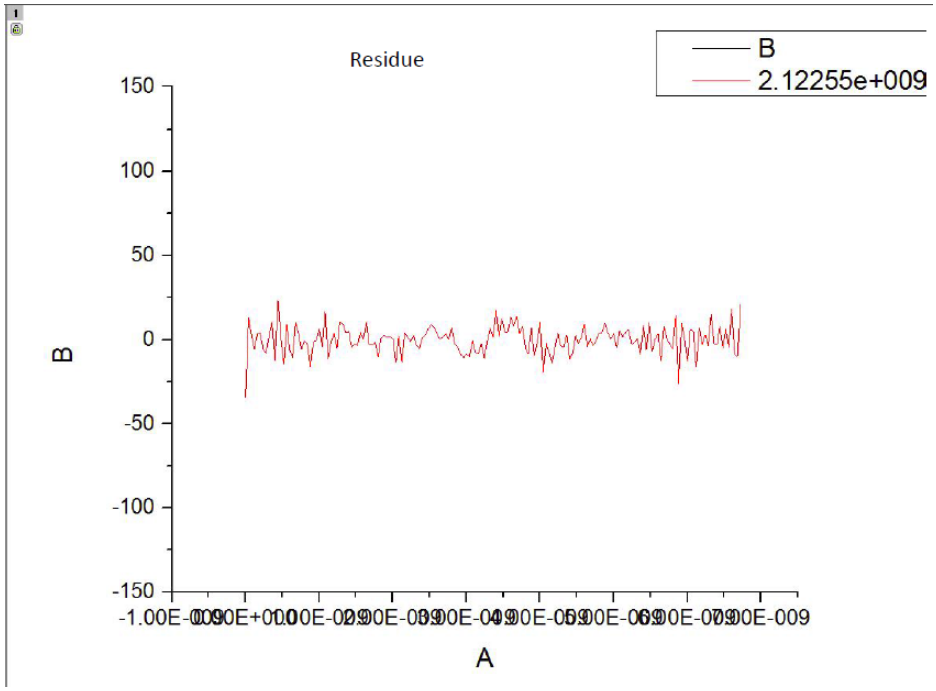

Figure A.11 Total Residual

Finally, all velocity information interested (Fp8, Diamond, Neon, and Interfacial) in time and frequency (velocity) domain can be co-plotted. Lorenz function was used to fit the velocities.

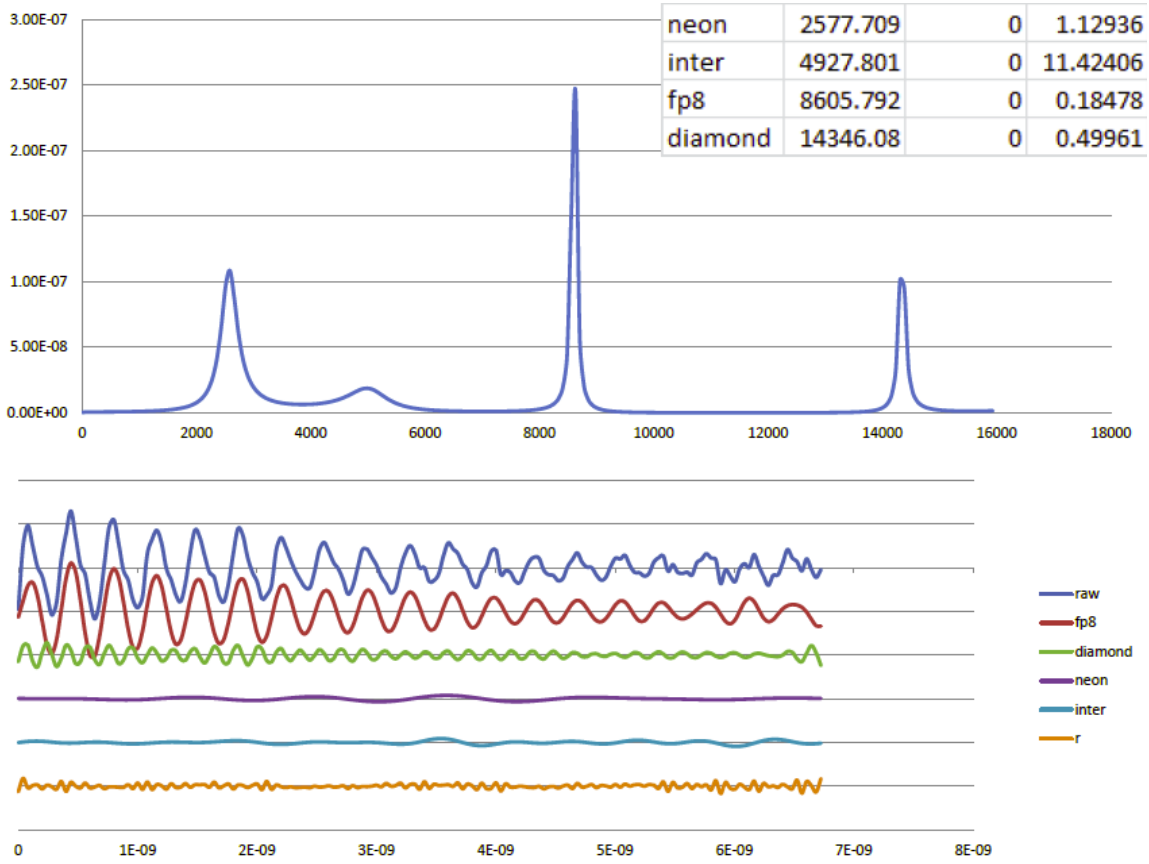

Figure A.12 All velocity information interested (fp8, diamond, neon, and interfacial) in time and frequency (velocity) domain are plotted. **The lower half** is in time domain which the unit in horizontal axis is second and the unit in vertical axis is arbitrary. From top to bottom, respectively, are the intensity modulation of original measurement, Fp8 Vp, Diamond, Neon, Interfacial wave, and residuals. **The upper half** is the power spectrum in velocity (frequency) domain. Units for horizontal and vertical axis are in m/s and arbitrary unit. Lorenz function was used to fit the velocities; from left to right, respectively, are the peaks for Neon, Interfacial wave, Fp8 Vp, and Diamond.

Appendix V Neon Velocities Data From ISS Measurement

Pressure		Neon			
P(GPa)	Error(GPa)	[100] (km/s)	Error (km/s)	[110] (km/s)	Error (km/s)
1.26	0.1	2.57770942	0.112936	2.82020798	0.324638
8.037	0.1	2.6524378	0.58875	2.11194698	0.407714
9.195	0.205	-	-	-	-
15.6	0.15	4.46209375	0.2448468	3.45954448	0.99223
16.4	0.15	4.08845186	0.6865636	3.05290324	0.7336955
55.24	0.8	6.22373586	0.282615	7.16267937	0.553999
67.27	0.37	6.86315842	1.5397161	6.33769123	0.4409699
70	1	6.81368785	0.4382661	-	-
75	1	7.05253096	0.45723	-	-
78	1	7.71638924	0.6760864	8.44459202	1.841097
83	1	8.31509887	2.636931	-	-
89	1	-	-	-	-

Appendix VI Diamond Velocities Data From ISS Measurement

Pressure		Diamond			
P(GPa)	Error(GPa)	[100] (km/s)	Error (km/s)	[110] (km/s)	Error (km/s)
1.26	0.1	14.34608491	0.49961	16.78388513	0.457582
8.037	0.1	17.51439262	1.81382	18.13361361	1.184335
9.195	0.205	17.39127081	0.25498	15.5023817	0.164019
15.6	0.15	18.00154687	0.2160309	19.28607053	0.46582
16.4	0.15	18.31784286	0.1740692	16.13046129	1.424386
55.24	0.8	18.98176527	1.35959	18.19062694	0.86217
67.27	0.37	18.3839848	0.48984	16.06639839	1.0244428
70	1	18.81086519	0.5371361	17.21350888	0.2854669
75	1	17.55902251	1.2528	17.19062375	0.8383755
78	1	18.42205642	0.592449	17.9851173	1.250997
83	1	18.47255966	0.657709	18.16690337	0.93673
89	1	18.60925994	0.75862	18.99801975	1.65805

References

Abramson, E.H., J.M. Brown, and L.J. Slutsky, (1999) Applications of impulsive stimulated scattering in the earth and planetary sciences, Ann. Rev. Phys. Chem., 50, 279-313

Badro, J., Rueff, J.-P., Vanko, G., Monaco, G., Fiquet, G., Guyot F. (2004), Electronic Transitions in Perovskite: Possible Nonconvecting Layers in the Lower Mantle, *Science* 305, 383

Birch, F., Finite strain isotherm and velocities for single-crystal and polycrystalline NaCl at high pressures and 300°K (1978), J. Geophys. Res., 83, B3,

Bower, Dan J., Gurnis, Michael, Jackson, Jennifer M., Sturhahn, Wolfgang, Enhanced convection and fast plumes in the lower mantle induced by the spin transition in ferropericlase, Geophys. Res. Lett.36 10 1944-8007 http://dx.doi.org/10.1029/2009GL037706

Carpenter M.A. and Salje E. K.H., Elastic anomalies in minerals due to structural phase transitions (in Phase transitions in minerals; strain and elasticity) European Journal of Mineralogy(August 1998), 10(4):693-812

Crowhurst, J. C., J. M. Brown, A. F. Goncharov, and S. D. Jacobsen (2008), Elasticity of (Mg,Fe)O through the spin transition of iron in the lower mantle, Science, 319, 451–453.

Every A.G., General closed-form expressions for acoustic waves in elastically anisotropic solids (1980), Phys. Rev. B 22, 1746

Fei, Y., Zhang, L., Corgne, A., Watson, H.C., Ricolleau, A., Meng, Y., Prakapenka, V.B., 2007. Spin transition and equations of state of (Mg, Fe)O solid solutions. Geophys. Res. Lett. 34, L17307, doi:10.1029/2007GL030712.

Hirose, K. (2006), Postperovskite phase transition and its geophysical implications, Rev. Geophys., 44, RG3001, doi:10.1029/2005RG000186.

Irifune, T. (1994), Absence of an aluminous phase in the upper part of the Earth's lower mantle, Nature, 370, 131–133

Irifune, T., and M. Isshiki (1998), Iron partitioning in a pyrolite mantle and the nature of the 410-kmseismic discontinuity, Nature, 370,131–133.

Irifune, T., T. Shinmei, C. A. McCammon, N. Miyajima, D. C. Rubie, and D. J. Frost (2010), Iron partitioning and density changes of pyrolite in Earth's lower mantle, Science, 327, 193–195.

Jackson, J.M., Sinogeikin, S.V., Jacobsen, S.D., Reichmann, H.J., Mackwell, S.J., Bass, J.D., 2006. Single-crystal elasticity and sound velocities of (Mg0.94Fe0.06)O ferropericlase to 20 GPa. J. Geophys. Res. 111, B09203.

Jacobsen, S.D., Reichmann, H.J., Spetzler, H., Mackwell, S.J., Smyth, J.R., Angel, R.J., McCammon, C.A., 2002. Structure and elasticity of single-crystal (Mg,Fe)O and a new method of generating shear waves for gigahertz ultrasonic interferometry.J. Geophys. Res. 107, 2037.

Lin, J. F., and T. Tsuchiya(2008), Spin transition of iron in the Earth's lower mantle, Phys. Earth Planet. Inter., 170, 248–259.

Lin, J. F., Struzhkin, V. V., Jacobsen, S. D., Hu, M., Chow, P., Kung, J., Liu, H., Mao, H. K., and Hemley, R. J., (2005), Spin transition of iron in magnesiowüstite in Earth's lower mantle, Nature, 436, 377-380

Lin, J.-F., Vanko, G., Jacobsen, S.D., Iota, V., Struzhkin, V.V., Prakapenka, V.B., Kuznetsov, A., Yoo, C.-S. Spin transition zone in Earth's lower mantle Science, 317 (2007), pp. 1740–1743

Lin, J.-F., S. Speziale, Z. Mao, and H. Marquardt (2013), Effects of the electronic spin transitions of iron in lower mantle minerals: Implications for deep mantle geophysics and geochemistry, Rev. Geophys., 51, 244–275, doi:10.1002/rog.20010.

Lu, C., Mao, Z., Lin, J.F., Zhuravlev, K. K., Tkachev, N. S., Prakapenka, B. V., Elasticity of single-crystal iron-bearing pyrope up to 20 GPa and 750 K, Earth and Planetary Science Letters 361 (2013) 134-142

Marquardt, H., Speziale, S., Reichmann, H. J., Frost, D. J., Schilling, F. R., 2009a. Single-crystal elasticity of (Mg0.9Fe0.1)O to 81 GPa. Earth and Planetary Science Letters 287 (2009) 345–352

Marquardt, H., Speziale, S., Reichmann, H. J., Frost, D. J., Schilling, F. R., and Garnero, E. J., 2009b, Elastic shear anisotropy of ferropericlase in Earth's lower mantle, Science, 324, 224–226.

Murakami, M., K. Hirose, K. Kawamura, N. Sata, and Y. Ohishi (2004), Post-perovskite phase transition in $MgSiO_3$, Science, 304,855–858.

Murakami, M., Y. Ohishi, N. Hirao, and K. Hirose (2012), A perovskitic lower mantle inferred from high-pressure, high-temperature sound velocity data, Nature, 485, 90–95.

Nelson, K. A., Fayer, M. D., (1980), Laser induced phonons: Aprobe of intermolecular in molecular solids, L,Chem. Phys, 72(9).

Nelson, K.A., Lutz, D.R., Fayer, M. D., Madison, L., (1981), Laser-induced phonon spectroscopy. Optical generation of ultrasonic waves and investigation of electronic excited-state interactions insolids

Oganov, A. R. and S. Ono (2004), Theoretical and experimental evidence for a post-perovskite phase of $MgSiO_3$ in Earth's D″ layer,Nature, 430, 445–448.

Ostwald, J., Pazold, W., Weis, O., 1977. High-resolution Brillouin spectroscopy of water. Appl. Phys. 13, 351-356

Polian, A., Vo-Thanh, D., Richet, P., 2002. Elastic properties of α-SiO_2 up to 3200 K from Brillouin scattering measurements. Europhys. Lett. 57, 375.

Ringwood, A. E. (1982), Phase transformations and differentiation in subducted lithosphere: Implications for mantle dynamics basalt petrogenesis and crustal evolution, J. Geol., 90, 611–642.

Sinogeikin, S.V., Bass, J.D., 2000. Single-crystal elasticity of pyrope and MgO to 20 GPa by Brillouin scattering in he diamond cell. Phys. Earth Planer. Inter. 120, 43-62

Sturhahn, W., Jackson, J.M., Lin, J.-F., The spin state of iron in minerals of Earth's lower mantle Geophys. Res. Lett., 32 (2005), p. L12307

Tange, Y., Nishihara Y., Tsuchiya T., Unified analyses for P-V-T equation of state of MgO: A solution for pressure-scale problems in high P-T experiments, J. Geophys. Res.114 B3 2156-2202 http://dx.doi.org/10.1029/2008JB005813

Tsuchiya, T., R. M. Wentzcovitch, C. R. S. da Silva, and S. deGironcoli (2006), Spin transition in magnesiowüstite in Earth's lower mantle, Phys. Rev. Lett., 96, 198501, doi:10.1103/PhysRevLett.96.198501.

Wentzcovitch, R. M., J. F. Justo, Z. Wu, C. R. S. da Silva, D. A. Yuen, and D. Kohlstedt (2009), Anomalous compressibility of ferropericlase throughout the iron spin cross-over, Proc. Natl. Acad. Sci. U. S. A., 106, 8447–8452.

Wu, Z., Justo, F. F., Wentzcovitch, R. M., Elastic Anomalies in a Spin-Crossover System: Ferropericlase at Lower Mantle Conditions (2013), Phys. Rev. Lett., 110, 228501

Yan, Y. X., Nelson, K. A., 1987, Impulsive stimulated light scattering. I. General theory. J. Chem. Phys. 87, 6240 (1987); http://dx.doi.org/10.1063/1.453733

Yang, Jing, Z. Mao, J.-F. Lin, B. P. Vitali (2014), Single-crystal elasticity of the deep-mantle magnesite at high pressure and temperature, Earth and Planetary Science Letters 392 (2014) 292–299

Zhang, Zhiying and Koppensteiner, Johannes and Schranz, Wilfried and Carpenter, Michael A (2012) Variations in elastic and anelastic properties of Co3O4 due to magnetic and spin state transitions. American Mineralogist, 97 (2-3). pp. 399-406.